

DETERMINING THE COSMIC DISTANCE SCALE FROM INTERFEROMETRIC MEASUREMENTS OF THE SUNYAEV-ZELDOVICH EFFECT

ERIK D. REESE,^{1,2,3} JOHN E. CARLSTROM,¹ MARSHALL JOY,⁴ JOSEPH J. MOHR,⁵ LAURA GREGO,⁶
 AND WILLIAM L. HOLZAPFEL²

Received 2002 May 16; accepted 2002 August 9

ABSTRACT

We determine the distances to 18 galaxy clusters with redshifts ranging from $z \sim 0.14$ to 0.78 from a maximum likelihood joint analysis of 30 GHz interferometric Sunyaev-Zeldovich effect (SZE) and X-ray observations. We model the intracluster medium (ICM) using a spherical isothermal β model. We quantify the statistical and systematic uncertainties inherent to these direct distance measurements, and we determine constraints on the Hubble parameter for three different cosmologies. These distances imply a Hubble constant of 60^{+4+13}_{-4-18} km s⁻¹ Mpc⁻¹ for an $\Omega_M = 0.3$, $\Omega_\Lambda = 0.7$ cosmology, where the uncertainties correspond to statistical followed by systematic at 68% confidence. With a sample of 18 clusters, systematic uncertainties clearly dominate. The systematics are observationally approachable and will be addressed in the coming years through the current generation of X-ray satellites (*Chandra* and *XMM-Newton*) and radio observatories (Owens Valley Radio Observatory, Berkeley-Illinois-Maryland Association, and Very Large Array). Analysis of high-redshift clusters detected in future SZE and X-ray surveys will allow a determination of the geometry of the universe from SZE-determined distances.

Subject headings: cosmic microwave background — cosmology: observations — distance scale — galaxies: clusters: general — techniques: interferometric

On-line material: color figures

1. INTRODUCTION

Analysis of Sunyaev-Zeldovich effect (SZE) and X-ray data provides a method of directly determining distances to galaxy clusters at any redshift. Clusters of galaxies contain hot ($k_B T_e \sim 10$ keV) gas, known as the intracluster medium (ICM), trapped in their potential wells. Cosmic microwave background (CMB) photons passing through a massive cluster interact with the energetic ICM electrons with a $\tau \approx 0.01$ probability. This inverse Compton scattering preferentially boosts the energy of a scattered CMB photon, causing a small ($\lesssim 1$ mK) distortion in the CMB spectrum, known as the SZE (Sunyaev & Zeldovich 1970, 1972). The SZE appears as a decrement for frequencies $\lesssim 218$ GHz and as an increment for frequencies $\gtrsim 218$ GHz. The SZE is proportional to the pressure integrated along the line of sight $\Delta T \propto \int n_e T_e dl$. X-ray emission from the ICM has a different dependence on the density $S_X \propto \int n_e^2 \Lambda_{eH} dl$, where Λ_{eH} is the X-ray cooling function. Taking advantage of the different density dependencies and with some assumptions about the geometry of the cluster, the distance to the cluster may be determined. SZE- and X-ray-determined distances are independent of the extragalactic distance ladder and provide distances to high-redshift galaxy clusters. The

promise of direct distances has been one of the primary motivations for SZE observations.

In the last decade, SZE detections have become routine as a result of advances in both instrumentation and observational strategy. Recent high signal-to-noise ratio (S/N) detections have been made with single-dish observations at radio wavelengths (Birkinshaw & Hughes 1994; Herbig et al. 1995; Myers et al. 1997; Hughes & Birkinshaw 1998), millimeter wavelengths (Holzapfel et al. 1997a, 1997b; Poin-tecou-teau et al. 1999, 2001), and submillimeter wavelengths (Lamarre et al. 1998; Komatsu et al. 1999). Interferometric observations at centimeter wavelengths are now routinely producing high-quality images of the SZE (Jones et al. 1993, 2002; Grainge et al. 1993, 2002b; Carlstrom, Joy, & Grego 1996; Carlstrom et al. 1998, 2000; Saunders et al. 1999; Reese et al. 2000; Grego et al. 2000, 2001).

In this paper we present a maximum likelihood joint analysis of our 30 GHz interferometric SZE observations with archival *ROSAT* X-ray imaging observations. Cluster X-ray temperatures, metallicity, and H I column densities are taken from the literature. The ICM is modeled as a spherical isothermal β model. We refine the analysis technique described in Reese et al. (2000) and apply it to a sample of 18 clusters for which we determine distances. These distances are then used to measure the Hubble constant. This is the largest homogeneously analyzed sample of SZE clusters with distance determinations thus far. To date, there are about 20 published estimates of H_0 based on combining X-ray and SZE data for individual clusters (see Birkinshaw 1999 for a review and compiled distances). Most notably, those results include one sample consisting of seven nearby ($z < 0.1$) galaxy clusters (Mason, Myers, & Readhead 2001; Mason 1999; Myers et al. 1997) and a sample of five intermediate-redshift ($0.14 < z < 0.3$) clusters (Jones et al. 2002).

¹ Department of Astronomy and Astrophysics, University of Chicago, 5640 South Ellis Avenue, Chicago, IL 60637.

² Department of Physics, University of California, Berkeley, CA 94720.

³ Chandra Fellow.

⁴ Space Science Laboratory, SD50, NASA Marshall Space Flight Center, Huntsville, AL 35812.

⁵ Department of Astronomy and Department of Physics, University of Illinois, Urbana, IL 61801.

⁶ Harvard-Smithsonian Center for Astrophysics, 60 Garden Street, Cambridge, MA 02138.

The cluster sample selection for this paper is discussed in § 2. The centimeter-wave SZE system and interferometric SZE data are described in § 3.1. A brief overview of the *ROSAT* X-ray cluster data is given in § 3.2. The analysis method, including uncertainty estimation, is outlined in § 4 along with the model fitting results. Distances and our determination of the Hubble parameter appear in § 5. Sources of possible systematic uncertainties are discussed in § 6. Section 7 contains a discussion of the results and future prospects. Throughout this work, the galaxy cluster Cl 0016+16 ($z = 0.546$) will be used as the example cluster to illustrate both the analysis method and general results. All uncertainties are 68.3% confidence unless explicitly stated otherwise.

2. CLUSTER SAMPLE

The determination of the Hubble parameter requires a large sample of galaxy clusters free of selection effects. For example, clusters selected by X-ray surface brightness will preferentially include clusters elongated along the line of sight. A spherical analysis will underestimate the line-of-sight length of the cluster, causing the derived Hubble parameter to be biased low. In theory, selecting by X-ray luminosity, L_X , alleviates the selection bias problem. In practice, this is complicated by the fact that X-ray surveys are surface brightness limited; clusters just at the detection limit that are elongated along the line of sight will be detected, while clusters just at the detection limit that are instead extended in the plane of the sky will be missed. Staying well above the detection limit of the survey will alleviate this potential pitfall. Observational considerations for cluster sample selection include the declinations of the clusters, the size (redshift) of the cluster, possible radio point sources in the cluster field, and SZE brightness for which we use L_X as an indicator. The Owens Valley Radio Observatory (OVRO) and Berkeley-Illinois-Maryland Association (BIMA) interferometers have been used to observe known X-ray clusters with $z \gtrsim 0.14$, $\text{decl.} \gtrsim -15^\circ$, and $L_X \gtrsim 5 \times 10^{44} h_{50}^{-2} \text{ ergs s}^{-1}$ (0.3–3.5 keV band for *Einstein* and 0.1–2.4 keV band for *ROSAT*). In addition, short, preliminary observations of many clusters are also performed to investigate possible point sources in the field.

The OVRO/BIMA SZE imaging project initially chose targets from the limited number of known X-ray-bright clusters. With the publishing of X-ray cluster surveys, the OVRO/BIMA SZE imaging project chose targets from three X-ray catalogs of galaxy clusters: the *Einstein Observatory* Extended Medium Sensitivity Survey (EMSS; Gioia et al. 1990; Stocke et al. 1991; Gioia & Luppino 1994; Maccacaro et al. 1994), the *ROSAT* X-Ray Brightest Abell Clusters (XBACs; Ebeling et al. 1996a, 1996b), and the *ROSAT* Brightest Cluster Sample (BCS; Ebeling et al. 1997, 1998, 2000a; Crawford et al. 1999). We have also recently included two more recent *ROSAT* samples of distant massive clusters to our cluster selection database: the Wide Angle *ROSAT* Pointed Survey (WARPS; Fairley et al. 2000; Ebeling et al. 2000b; Jones et al. 1998; Scharf et al. 1997) and the Massive Cluster Survey (MACS; Ebeling, Edge, & Henry 2001). So far, we have high-S/N detections in 21 clusters with redshifts $z > 0.45$.

The distance calculation requires three data sets: SZE, X-ray imaging, and X-ray spectroscopic data. We have obtained high-S/N detections of the SZE in 45 galaxy

clusters. The subsample of these clusters that also have high-S/N X-ray imaging data and published electron temperatures contains 18 galaxy clusters. Table 1 summarizes the redshifts and X-ray luminosities for each galaxy cluster in our sample.

3. DATA

Here we briefly describe the SZE and X-ray observations and data reduction. Table 2 summarizes the observation times for both the SZE and *ROSAT* observations of each cluster in our sample. The SZE observation times are the total on-source integration times for the interferometric SZE data used in this analysis. The *ROSAT* observation times are the total live times of the pointings used in this analysis.

3.1. Interferometric SZE Data

The extremely low systematics of interferometers make them well suited to study the weak SZE signal. A unique feature of interferometers is their ability to separate the diffuse, negative SZE emission from small-scale, positive point-source emission through the spatial filtering of the interferometer. Interferometers also provide a well-defined angular and spectral filter, which is important in the analysis of the SZE data discussed in § 4.

3.1.1. Centimeter-Wave System and Observing Strategy

Over the past several summers, we outfitted the BIMA millimeter array in Hat Creek, California, and the OVRO millimeter array in Big Pine, California, with centimeter wavelength receivers. Our receivers use cooled (~ 10 K) High Electron Mobility Transistor (HEMT) amplifiers (Pospieszalski et al. 1995) operating over 26–36 GHz with characteristic receiver temperatures of $T_{\text{rx}} \sim 11$ –20 K over the 28–30 GHz band used for the observations presented here. When combined with the BIMA or OVRO systems, these receivers obtain typical system temperatures scaled to above the atmosphere of $T_{\text{sys}} \sim 35$ –45 K. Most telescopes are placed in a compact configuration to maximize sensitivity on angular scales subtended by distant clusters ($\sim 1'$), but telescopes are always placed at longer baselines for simultaneous detection of point sources. Every half-hour we observe a bright quasar, commonly called a phase calibrator, for about 2 minutes to monitor the system phase and gain. The total integration time for each cluster field is given in Table 2 for both OVRO and BIMA.

An interferometer samples the Fourier transform of the sky brightness distribution multiplied by the primary beam rather than the direct image of the sky. The SZE data files include the positions in the Fourier domain, which depend on the arrangement of the telescopes in the array and the declination of the source, the real and imaginary Fourier components, and a measure of the noise in the real and imaginary components. The Fourier conjugate variables to right ascension and declination are commonly called u and v , respectively, and the Fourier domain is commonly referred to as the u - v plane. The real and imaginary Fourier component pairs as a function of u and v are called visibilities.

The finite size of each telescope dish results in an almost Gaussian response pattern, known as the primary beam. The product of the primary beam and the sky brightness

TABLE 1
CLUSTER SAMPLE

Cluster	Redshift	L_X^a ($\times 10^{44} h_{50}^{-2} \text{ ergs s}^{-1}$)	Band (keV)	References (z, L_X)
MS 1137.5+6625	0.784	5.4	0.3–3.5	1, 2
MS 0451.6–0305	0.550	20.0	0.3–3.5	2, 2
Cl 0016+16	0.546	14.6	0.3–3.5	3, 2
RX J1347.5–1145	0.451	73.0	0.1–2.4	4, 5
A370	0.374	11.7 ^b	0.1–2.4	6, 7
MS 1358.4+6245	0.327	10.6	0.3–3.5	2, 2
A1995	0.322	13.4	0.1–2.4	8, 9
A611	0.288	8.6	0.1–2.4	10, 9
A697	0.282	19.2	0.1–2.4	10; 9, 11
A1835	0.252	32.6	0.1–2.4	12; 9, 11
A2261	0.224	20.6	0.1–2.4	10, 9
A773	0.216	12.1	0.1–2.4	12; 9, 11
A2163	0.202	37.5	0.1–2.4	12, 13
A520	0.202	14.5	0.1–2.4	2; 9, 11
A1689	0.183	20.7	0.1–2.4	14, 13
A665	0.182	15.7	0.1–2.4	14, 9
A2218	0.171	8.2	0.1–2.4	15, 9
A1413	0.142	10.9	0.1–2.4	12; 9, 11

^a Computed for a flat $\Omega_M = 1$ universe.

^b Converted the 2–10 keV flux in Arnaud & Evrard 1999 to the 0.1–2.4 keV band (approximate factor of 0.9 determined from cooling function calculation).

REFERENCES.—(1) Donahue et al. 1999. (2) Gioia & Luppino 1994. (3) Dressler & Gunn 1992. (4) Schindler et al. 1995. (5) Schindler et al. 1997. (6) Mellier et al. 1988. (7) Arnaud & Evrard 1999. (8) Patel et al. 2000. (9) Böhringer et al. 2000. (10) Crawford et al. 1995. (11) Ebeling et al. 1998. (12) Struble & Rood 1999. (13) Ebeling et al. 1996a. (14) Struble & Rood 1991. (15) Le Borgne, Pello, & Sanahuja 1992.

distribution is equivalent to a convolution in the Fourier domain. The primary beams are measured using holography data for both OVRO and BIMA. The main lobes of the primary beams are well fitted by a Gaussian with an FWHM of 4.2 for OVRO and 6.6 for BIMA at 28.5 GHz.

However, we use the measured primary beam profiles for our analysis.

The primary beam sets the field of view. The effective resolution, called the synthesized beam, depends on the sampling of the u - v plane and is therefore a function of the

TABLE 2
CLUSTER DATA

CLUSTER	INTERFEROMETRIC SIZE DATA								<i>ROSAT</i> DATA	
	OVRO (hr)				BIMA (hr)				PSPC (ks)	HRI (ks)
	1994	1995	1996	1998	1996	1997	1998	2000		
MS 1137	40	48	99.1
MS 0451	30	15.4	45.9
Cl 0016	87	13	29 ^a	8	41.6	70.2
R1347	20.0	...	36.1
A370	33	26	31.9
MS 1358	9	7	70	...	22.1	29.2
A1995	58	50	37.6
A611	45	12	17.2
A697	47	27.8
A1835	27	...	8.5	2.8
A2261	40	3	16.1
A773	57	9	5 ^a	...	18	16.5
A2163	25	12	2	10	11	...	11.7	35.8
A520	7	13 ^a	23	20	...	4.7	12.6
A1689	26	16	13.5	22.5
A665	38 ^a	24	37.0	98.3
A2218	64	6	...	20 ^a	12	42.5	35.5
A1413	11	17	7.5	18.6

^a Contains 1996 BIMA data with delay loss problem; data only used to make images and not in the analysis.

configuration of the telescopes and the declination of the source. The cluster SZE signal is largest on the shortest baselines (largest angular scales). The shortest possible baseline is set by the diameter of the telescopes, D . Thus, the system is not sensitive to angular scales larger than about $\lambda/2D$, which is ~ 2.8 for BIMA observations and ~ 1.7 for OVRO observations. The compact configuration used for our observations yields significant SZE signal at these angular scales but filters out signal on larger angular scales. Because of the spatial filtering by the interferometer, it is necessary to fit models directly to the data in the u - v plane, rather than to the deconvolved image.

Interferometers simultaneously measure both the cluster signal and the point sources in the field. The SZE signal is primarily present in the short baseline data, while the response of an interferometer to a point source is independent of the baseline. Therefore, observations with a range of baselines allow us to separate the extended cluster emission from point-source emission. We show an example of this after first presenting details of deconvolved 30 GHz images (for additional examples see Jones et al. 1993; Carlstrom et al. 2000).

3.1.2. Data Reduction

The data are reduced using the MIRIAD (Sault, Teuben, & Wright 1995) software package at BIMA and using MMA (Scoville et al. 1993) at OVRO. In both cases, data are excised when one telescope is shadowed by another, when cluster data are not straddled by two phase calibrators, when there are anomalous changes in instrumental response between calibrator observations, or when there is spurious correlation. For absolute flux calibration, we use observations of Mars and adopt the brightness temperature from the Rudy (1987) Mars model. For observations not containing Mars, calibrators in those fields are bootstrapped back to the nearest Mars calibration (for more details see Grego et al. 2001). The observations of the phase calibrators over each summer give us a summer-long calibration of the gains of the BIMA and OVRO interferometers. They both show very little gain variation, changing by less than 1% over a many-hour track, and the average gains remain stable from day to day. In fact, the gains are stable at the $\sim 1\%$ level over a period of months.

3.1.3. Data Visualization: 30 GHz Images

Here we present deconvolved images of our 30 GHz interferometric observations. However, we stress that these images are made to demonstrate the data quality. The model fitting is performed in the Fourier plane, where the noise characteristics of the data and the spatial filtering of the interferometer are well understood. We first discuss point source identification and present high-resolution GHz images in Figure 1, and then present SZE images overlaid on X-Ray data in Figure 2. The SZE and X-ray image overlays of Figure 2 show that the region of the cluster sampled by the interferometric SZE observations and the X-ray observations is similar for the clusters in our sample. In addition, the interferometer measures a range of angular scales, which is not apparent from the images in Figure 2. Images showing examples of our SZE data at varying resolutions appear in Carlstrom et al. (1996) for Cl 0016 and Carlstrom et al. (2000) for R1347.

Point sources are identified from SZE images created with DIFMAP (Pearson et al. 1994) using only the long-baseline data ($\gtrsim 2000 \lambda$) and natural weighting (σ^{-2} weight).

Approximate positions and fluxes for each point source are obtained from this image and used as inputs for the model fitting discussed in § 4.2. The data are separated by observatory, frequency, and year to allow for temporal and spectral variability of the point-source flux. The positions and fluxes of the detected point sources from the model fitting are summarized in Table 3. Also listed are the corresponding 1.4 GHz fluxes for these sources from the NRAO VLA Sky Survey (NVSS; Condon et al. 1998) and the 5 and 15 GHz fluxes for sources in the three cluster fields surveyed by Moffet & Birkinshaw (1989). The uncertainty in the positions of the point sources is roughly $\pm 3''$ at 68.3% confidence based on model fits of point sources described in § 4.2. Figure 1 shows the 30 GHz high-resolution ($\gtrsim 2000 \lambda$) maps (*gray scale*) with NVSS 1.4 GHz contours. The gray-scale wedge above each image shows the range in the map in units of mJy beam $^{-1}$. Contours are multiples of twice the NVSS rms (rms ~ 0.45 mJy beam $^{-1}$). The FWHM of the 30 GHz synthesized beam is shown in the lower left-hand corner of each panel, and the 45'' FWHM beam of the NVSS is shown in the lower right-hand corner of each panel. Table 4 summarizes the sensitivity and the FWHM of the synthesized beam of the high-resolution maps used to find point sources in each field and shown in Figure 1.

Figure 2 shows the deconvolved SZE image contours overlaid on the X-ray images for each cluster in our sample. Negative contours are shown as solid lines, and the contours are multiples of twice the rms of each image. The images for MS 0451 and Cl 0016 have been published previously (Reese et al. 2000), but we include them here so that the entire sample appears together. We use DIFMAP (Pearson et al. 1994) to produce the naturally weighted SZE images. If any point sources are detected in the cluster field, they are subtracted from the data and a Gaussian taper applied to the visibilities to emphasize brightness variations on cluster scales before the image is deconvolved (CLEANed). The half-power radius of the Gaussian taper applied varies between 1000 and 2000 λ , depending on the observatory and telescope configurations used during the observations. Typically a 1000 λ half-power radius taper is applied to BIMA data and a 2000 λ half-power radius taper is applied to OVRO data. The FWHM of the synthesized (restoring) beam is shown in the lower left-hand corner of each image. Table 4 summarizes the rms sensitivities and the FWHMs of the synthesized beams of the tapered maps shown in Figure 2, as well as the corresponding statistics for the high-resolution ($\gtrsim 2000 \lambda$) images. In addition, Table 4 lists the Rayleigh-Jeans (RJ) brightness sensitivities for each tapered, deconvolved image.

3.1.4. Point-Source Identification Using Spatial Filtering

The identification and removal of point sources by taking advantage of the spatial filtering of the interferometer are illustrated in the panels of Figure 3 for the BIMA SZE Cl 0016 data. During the maximum likelihood joint analysis (see § 4.2), radio point sources identified from this procedure are modeled and fitted for directly in the u - v plane. Each panel covers the same angular region, roughly $20'$ on a side, and each panel shows the FWHM of the synthesized beam in the lower left-hand corner. Above each image is the gray-scale mapping showing the flux density of the map in units of mJy beam $^{-1}$. Figure 3a shows the “natural” image, which includes all of the data. There is smooth, extended,

TABLE 3
RADIO POINT SOURCES

Field	R.A. ^a (J2000.0)	Decl. ^a (J2000.0)	$F_{30.0}$ (mJy)	$F_{28.5}$ (mJy)	F_{15}^b (mJy)	F_5^b (mJy)	$F_{1.4}^c$ (mJy)
MS 1137.....
MS 0451.....	04 54 22.1	−03 01 25	1.41 ^{+0.26} _{−0.26}	1.86 ^{+0.26} _{−0.26}	14.9 ^{+0.7} _{−0.7}
CI 0016.....	00 18 31.1	16 20 45	...	9.11 ^{+1.97} _{−1.97}	25.0 ^{+1.5} _{−1.5}	84.5 ^{+1.1} _{−1.1}	269.3 ^{+8.1} _{−8.1}
R1347.....	13 47 30.7	−11 45 09	...	10.81 ^{+0.19} _{−0.19}	47.6 ^{+1.9} _{−1.9}
A370.....	02 39 55.5	−01 34 06	0.84 ^{+0.09} _{−0.09}	0.77 ^{+0.07} _{−0.07}	11.7 ^{+1.1} _{−1.1}
MS 1358.....	13 59 50.6	62 31 05	...	1.61 ^{+0.17} _{−0.17}
A1995.....	14 53 00.5	58 03 19	0.58 ^{+0.05} _{−0.05}	0.58 ^{+0.04} _{−0.04}	8.9 ^{+0.9} _{−0.9}
A611.....
A697.....
A1835.....	14 01 02.0	02 52 42	...	2.76 ^{+0.14} _{−0.14}	41.4 ^{+1.9} _{−1.9}
	14 01 00.5	02 51 53	...	1.16 ^{+0.15} _{−0.15}
A2261.....	17 22 17.1	32 09 14	10.10 ^{+0.24} _{−0.24}	10.80 ^{+0.24} _{−0.24}	24.3 ^{+1.6} _{−1.6}
A773.....
A2163.....	16 15 43.3	−06 08 40	1.44 ^{+0.12} _{−0.12}	1.44 ^{+0.08} _{−0.08}
A520.....	04 54 01.1	02 57 47	...	7.97 ^{+0.23} _{−0.23}	6.7 ^{+0.5} _{−0.5}
	04 54 17.0	02 55 32	...	1.01 ^{+0.10} _{−0.10}	15.3 ^{+1.1} _{−1.1}
	04 54 20.3	02 54 56	...	1.03 ^{+0.12} _{−0.12}	27.8 ^{+1.6} _{−1.6}
A1689.....	13 11 31.6	−01 19 33	1.33 ^{+0.10} _{−0.10}	1.51 ^{+0.09} _{−0.09}	61.0 ^{+2.5} _{−2.5}
	13 11 30.1	−01 20 37	0.45 ^{+0.09} _{−0.09}	0.42 ^{+0.09} _{−0.09}	10.9 ^{+0.6} _{−0.6}
A665.....	08 31 30.9	65 52 35	...	4.83 ^{+0.28} _{−0.28}	12.7 ^{+0.3} _{−0.3}	25.7 ^{+1.6} _{−1.6}	31.1 ^{+1.3} _{−1.3}
A2218.....	16 35 22.1	66 13 23	4.29 ^{+0.21} _{−0.21}	4.43 ^{+0.20} _{−0.20}	5.0 ^{+0.6} _{−0.6}	2.8 ^{+0.2} _{−0.2}	...
	16 35 47.7	66 14 46	1.36 ^{+0.10} _{−0.10}	1.59 ^{+0.11} _{−0.11}	2.4 ^{+0.6} _{−0.6}	3.7 ^{+0.3} _{−0.3}	18.0 ^{+1.8} _{−1.8}
	16 36 16.0	66 14 23	2.41 ^{+0.19} _{−0.19}	3.13 ^{+0.30} _{−0.30}	2.0 ^{+0.5} _{−0.5}	4.2 ^{+0.3} _{−0.3}	13.3 ^{+0.8} _{−0.8}
A1413.....	11 55 08.7	23 26 17	...	2.01 ^{+0.23} _{−0.23}	28.8 ^{+1.3} _{−1.3}

NOTE.—Units of right ascension are hours, minutes, and seconds, and units of declination are degrees, arcminutes, and arcseconds.

^a Positions from SZE observations.

^b From Moffet & Birkinshaw 1989.

^c From Condon et al. 1998.

TABLE 4
SZE IMAGE STATISTICS

CLUSTER	Observatory	TAPERED ^a			HIGH RESOLUTION ^b		
		σ ($\mu\text{Jy beam}^{-1}$)	Beam (arcsec)	σ_{RJ} (μK)	Observatory	σ ($\mu\text{Jy beam}^{-1}$)	Beam (arcsec)
MS 1137.....	BIMA	120	90 × 94	21	BIMA	105	20 × 24
MS 0451.....	OVRO	90	44 × 69	45	OVRO	60	19 × 25
CI 0016.....	BIMA	250	81 × 101	46	BIMA	220	14 × 30
R1347.....	BIMA	307 ^c	93 × 94 ^c	53 ^c	BIMA	245	17 × 27
A370.....	OVRO	60	56 × 86	19	OVRO	70	17 × 23
MS 1358.....	BIMA	140	96 × 98	22	BIMA	120	17 × 20
A1995.....	BIMA	134	70 × 77	37	OVRO	65	17 × 20
A611.....	OVRO	60	48 × 58	32	OVRO	45	20 × 39
A697.....	OVRO	65	50 × 53	37	OVRO	50	19 × 33
A1835.....	BIMA	213	87 × 121	30	BIMA	190	18 × 22
A2261.....	OVRO	85	49 × 53	49	OVRO	75	19 × 35
A773.....	BIMA	260	91 × 99	43	OVRO	90	19 × 26
A2163.....	BIMA	300	90 × 104	48	OVRO	85	19 × 30
A520.....	BIMA	180	90 × 101	30	OVRO	80	12 × 16
A1689.....	BIMA	320	93 × 94	55	OVRO	72	18 × 49
A665.....	BIMA	160	93 × 99	26	BIMA	150	16 × 26
A2218.....	BIMA	200	93 × 99	31	OVRO	50	21 × 22
A1413.....	BIMA	250	93 × 99	44	BIMA	210	16 × 26

^a Gaussian taper with FWHM of 2000 Å for OVRO data and 1000 Å for BIMA data.

^b Using only data with $(\mu^2 + v^2)^{1/2} > 2000 \lambda$.

^c Used Gaussian taper with FWHM of 1500 Å.

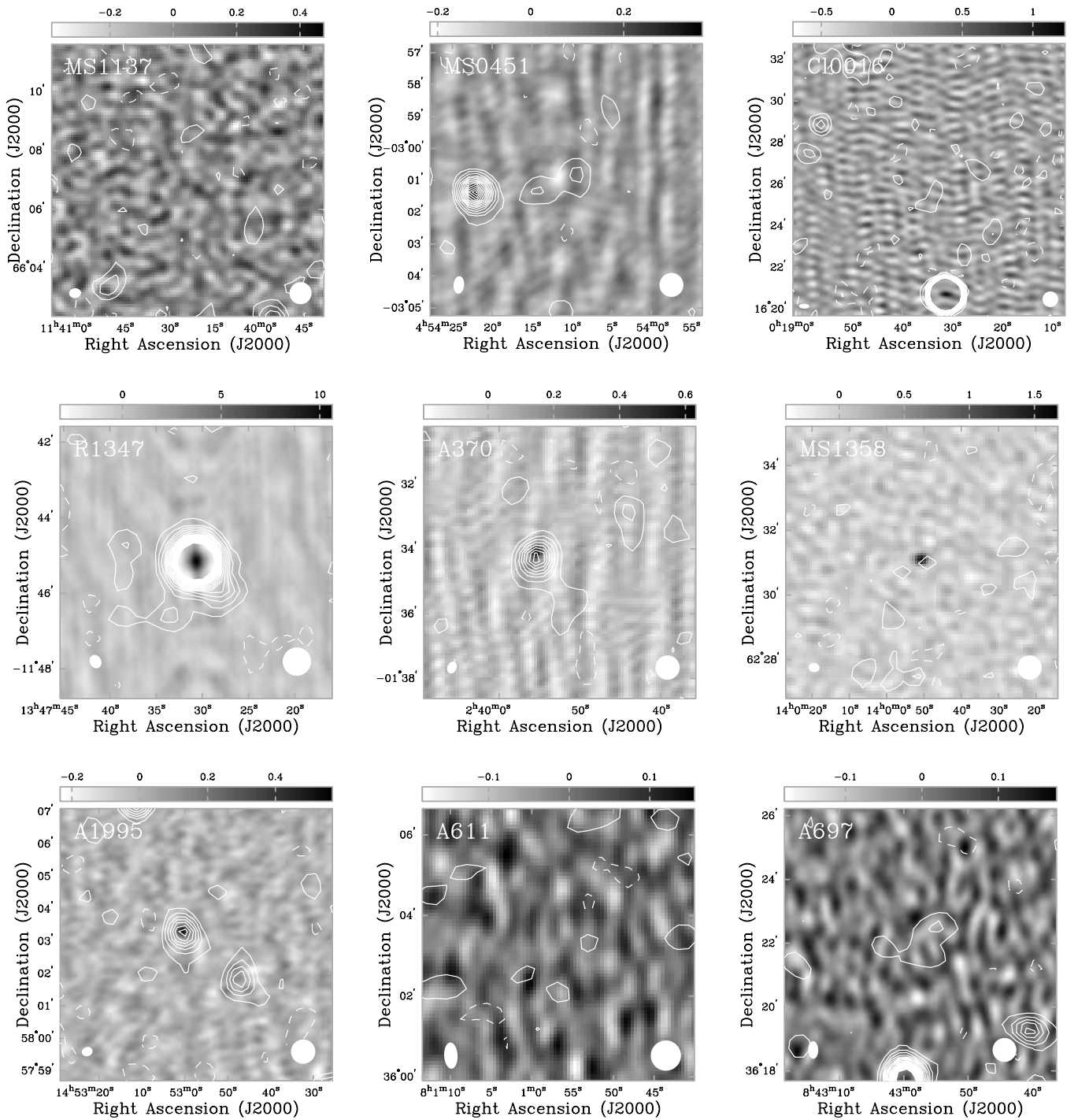
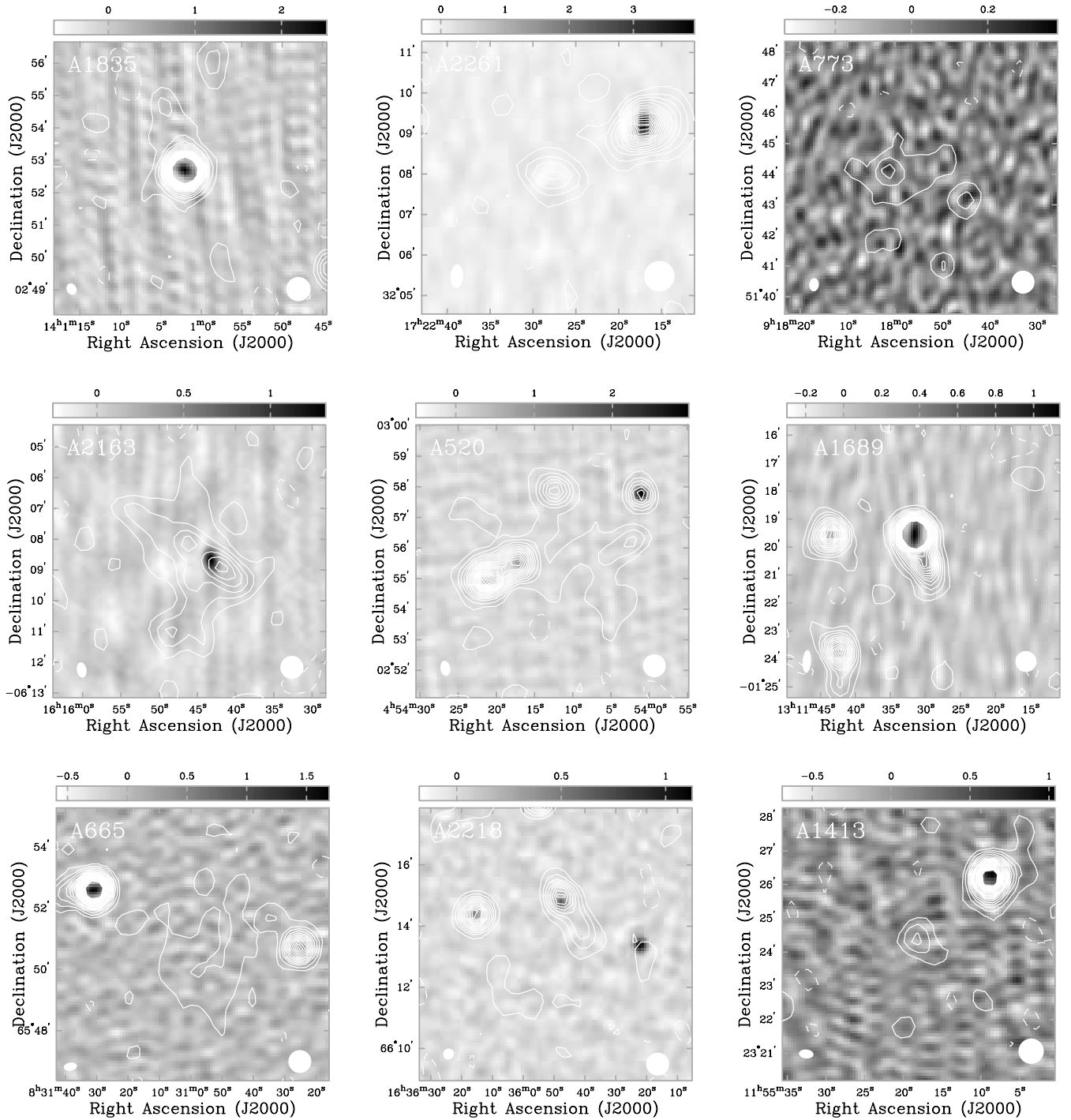


FIG. 1.—High-resolution ($\geq 2000 \lambda$) 30 GHz (gray scale) with NVSS 1.4 GHz contours. The gray-scale wedge above each image shows the range in the 30 GHz map in units of mJy beam^{-1} . Contours are multiples of twice the NVSS rms of $\sim 0.45 \text{ mJy beam}^{-1}$. The FWHM of the 30 GHz synthesized beam is shown in the lower left-hand corner of each panel, and the $45''$ FWHM beam of the NVSS is shown in the lower right-hand corner of each panel. The 30 GHz image statistics are summarized in Table 4. [See the electronic edition of the *Journal* for a color version of this figure.]

negative emission in the center of the map; this is the SZE decrement of C1 0016. There is also a bright spot roughly $2'$ south of the cluster that may be a point source. The large-scale symmetric pattern is the synthesized beam of the low-resolution data (compare to Fig. 3c); even when all baselines are considered, the SZE signal dominates. Figure 3b shows the high-resolution map using data with projected baselines $\geq 2000 \lambda$ only. The point source shows up easily now with the characteristic shape of the synthesized beam for these

data. We remove the point source by CLEANing. A Gaussian u - v taper (half-power radius of 1000λ) is then applied to the full data set to emphasize the short baselines, corresponding to the angular scales typical of galaxy clusters and shown in Figure 3c. The cluster is apparent as is the symmetric pattern of the synthesized beam. Deconvolving (CLEANing) the tapered image results in Figure 3d, which appeared in Figure 2 overlaid on X-ray data. The contours are multiples of twice the rms of the map.

FIG. 1.—*Continued*

3.2. *ROSAT* X-Ray Data

We use archival *ROSAT* data from both the Position Sensitive Proportional Counter (PSPC) and High Resolution Imager (HRI) instruments. The live times of the observations we use are listed in Table 2 for both PSPC and HRI observations.

3.2.1. Data Reduction

We use the Snowden Extended Source Analysis Software (ESAS; Snowden et al. 1994; Snowden 1998) to

reduce the data. We use the ESAS to generate a raw counts image, a noncosmic background image, and an exposure map for the HRI (0.1–2.4 keV) data and for each of the Snowden bands R4–R7 (PI channels 52–201; approximately 0.5–2.0 keV) for the PSPC data, using a master veto rate (a measure of the cosmic-ray and gamma-ray backgrounds) of 200 counts s^{-1} for the PSPC data. We examine the light-curve data of both instruments looking for time intervals with anomalously high count rates (short-term enhancements) and for periods of high scattered solar X-ray contamination. Contaminated

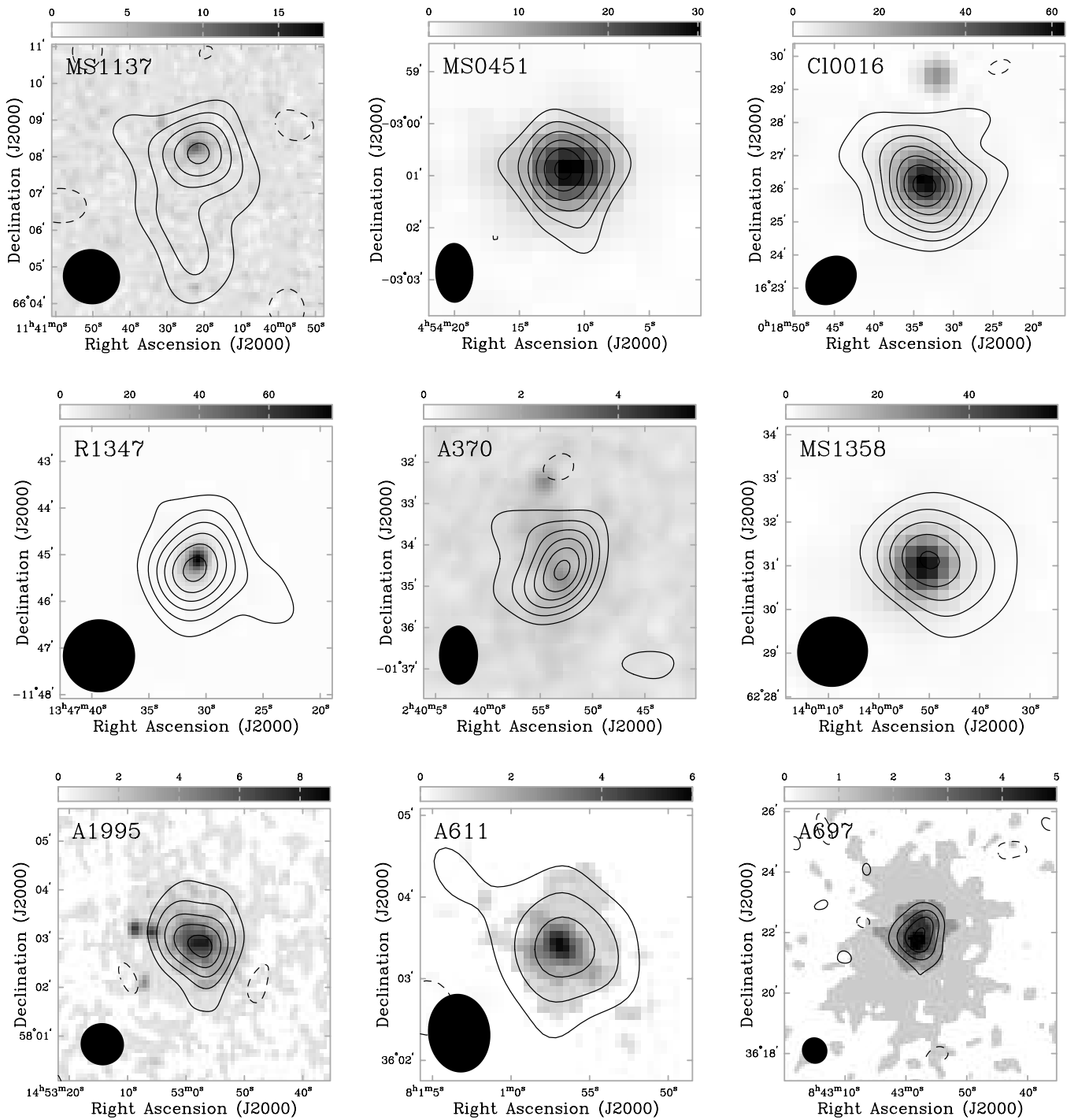


FIG. 2.—SZE (contours) and X-ray (gray scale) images of each cluster in our sample. Negative contours are shown as solid lines. The contours are multiples of 2σ , and the FWHMs of the synthesized beams are shown in the bottom left-hand corner. The X-ray gray-scale images are raw counts images smoothed with Gaussians with $\sigma = 15''$ for PSPC data and $\sigma = 5''$ for HRI data. There is a gray-scale mapping for the counts above each image. The 30 GHz image statistics are summarized in Table 4. [See the electronic edition of the *Journal* for a color version of this figure.]

and anomalously high count rate data are excised. The Snowden software produces 512×512 pixel images with $14''/947$ pixels for the PSPC and $5''/0$ pixels for the HRI. For the PSPC, final images for all of the R4–R7 bands together are generated by adding the raw counts images and the background images. Each Snowden band has a slightly different effective exposure map, and there is an energy dependence in the point-spread function (PSF). Thus, we generate a single exposure image and a single

PSF image by combining cluster photon-weighted averages of the four exposure images, and the four PROS (Worrall et al. 1992; Conroy et al. 1993) generated on-axis PSF images. The cluster photon weighting is determined using the background-subtracted detected photons within a circular region centered on the cluster. The region selected to construct the weights is the largest circular region encompassing the cluster that contains no bright point sources, typically a 15 pixel radius.

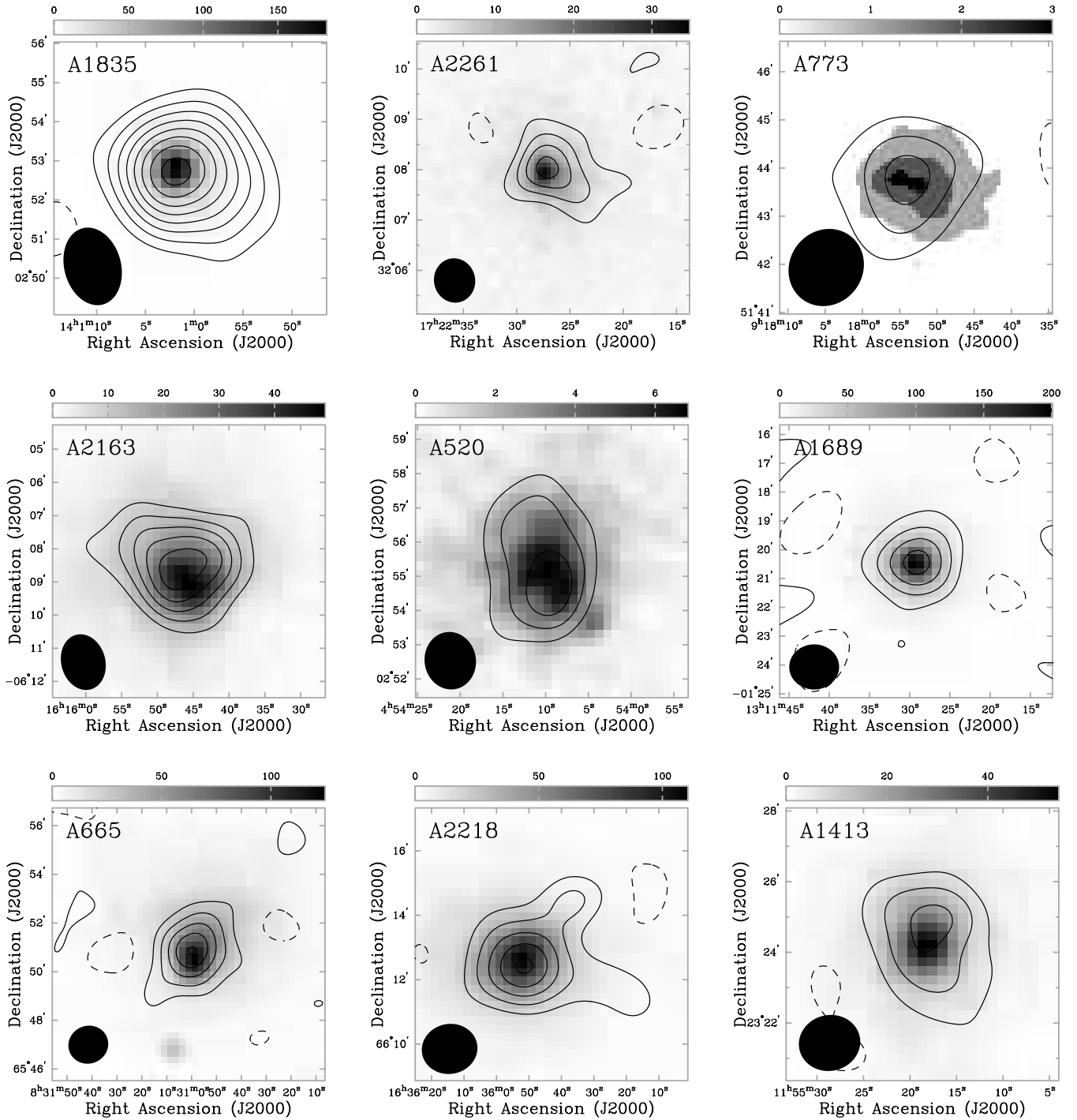


FIG. 2.—Continued

3.2.2. X-Ray Images and Data Properties

We show smoothed X-ray raw counts images in Figure 2 (gray) with SZE image contours overlaid. PSPC images are shown when available and HRI images otherwise. Table 2 summarizes the on-source integration time of the *ROSAT* observations of the clusters in our sample for both the PSPC and HRI. These images roughly contain a few thousand cluster counts. PSPC images are smoothed with Gaussians with $\sigma = 15''$ and HRI images with $\sigma = 5''$. The gray-scale wedge above each figure shows the mapping between color and detector counts.

3.2.3. X-Ray Spectral Data

We used published temperatures, metallicities, and H I column densities from observations with the *Advanced Satellite for Cosmology and Astrophysics (ASCA)*. Temperatures and metallicities for most of the clusters in our sample appear in Allen & Fabian (1998a, 1998b) and Allen (2000). When there is a detailed account of the analysis for a particular cluster, we use those results instead. When fitted metallicities are unavailable, we adopt a 0.2 solar metallicity with a 100% uncertainty. We use fitted H I column densities when available; otherwise,

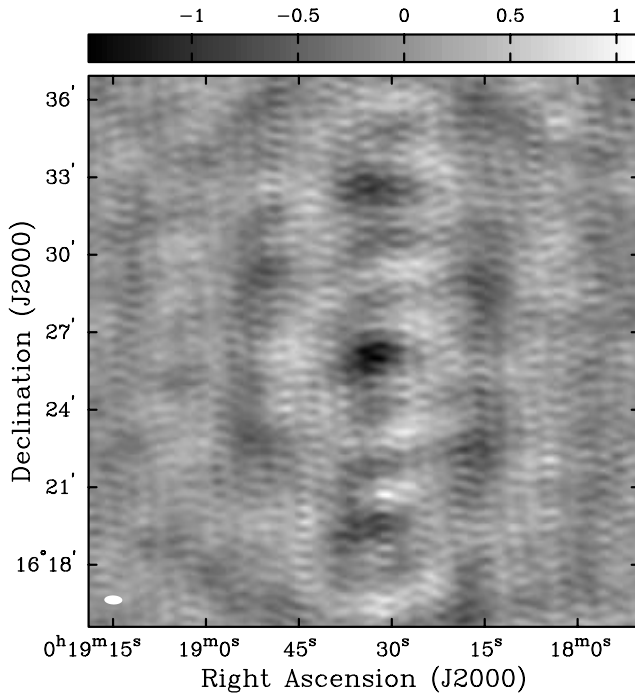


FIG. 3a

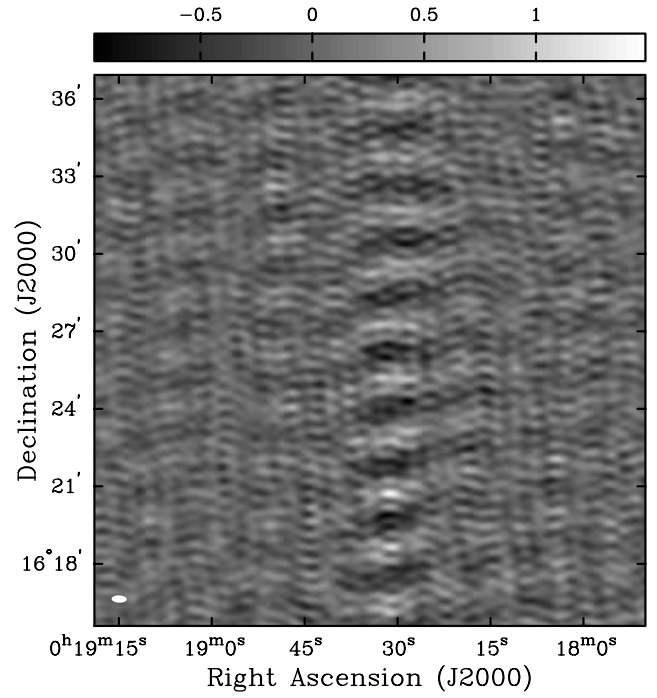


FIG. 3b

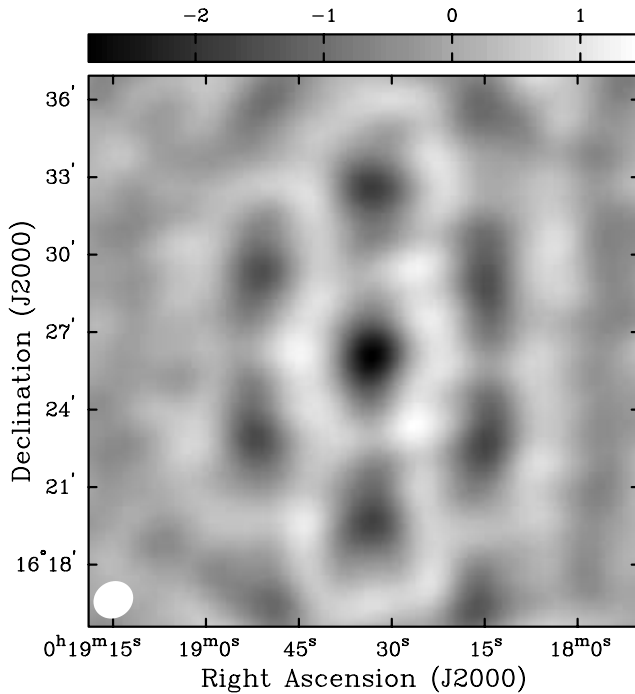


FIG. 3c

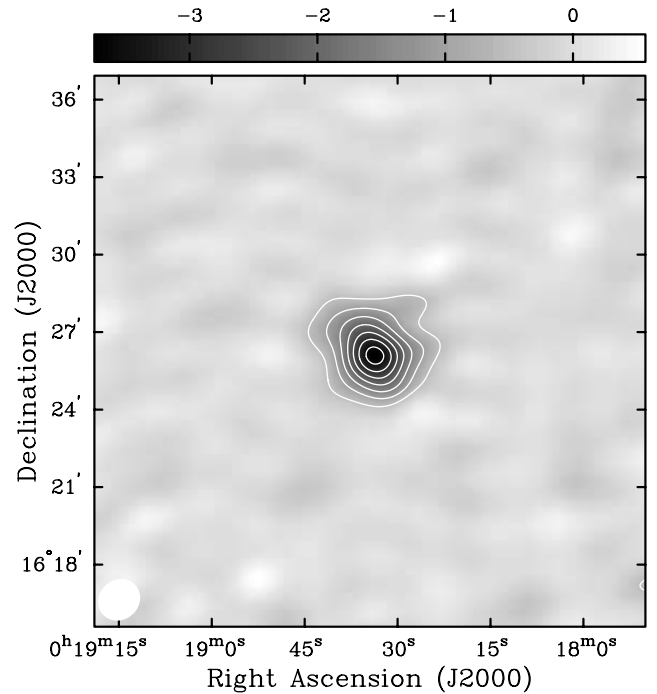


FIG. 3d

FIG. 3.—Panels illustrating how the spatial filtering of the interferometer is used to disentangle the point-source emission from the SZE emission. Each panel is roughly $20'$ on a side with the FWHM of the synthesized beam shown in the lower left-hand corner. The mapping of the gray scale is shown above each panel in units of mJy beam^{-1} . (a) “Natural”; (b) high resolution ($\geq 2000 \lambda$); (c) tapered map after point-source removal; (d) deconvolved SZE image (contours are multiples of 2σ). See text for details. [See the electronic edition of the Journal for a color version of this figure.]

those from 21 cm surveys of our Galaxy (Dickey & Lockman 1990) are adopted. We assign a conservative 50% uncertainty to the column densities adopted from 21 cm surveys of our Galaxy. Table 5 summarizes our adopted electron temperatures, metallicities, and column densities with references for the sources of this information.

Temperatures for many of our clusters also appear in Mushotzky & Scharf (1997). Multiple temperature determinations agree within the 1σ intervals for most of the clusters in our sample. The measurements overlap within 2σ in the worst cases, i.e., for the clusters MS 1358, A1995, A2163, A1689, and A1413. The temperatures, metallicity, column densities, and redshift of the cluster are used to determine

TABLE 5
X-RAY SPECTRAL INFORMATION

Cluster	kT_e (keV)	[Fe/H]	N_H ($\times 10^{20} \text{ cm}^{-2}$)	References (T_e , [Fe/H], N_H)
MS 1137.....	$5.7^{+1.3}_{-0.7}$	$0.43^{+0.26}_{-0.24}$	1.00 ^a	1, 1, 1
MS 0451.....	$10.4^{+1.0}_{-0.8}$	$0.15^{+0.07}_{-0.07}$	$3.00^{+0.40}_{-0.30}$	2, 2, 2
Cl 0016.....	$7.55^{+0.72}_{-0.58}$	$0.07^{+0.11}_{-0.07}$	$5.59^{+0.41}_{-0.36}$	3, 3, 3
R1347.....	$9.3^{+0.7}_{-0.6}$	$0.33^{+0.06}_{-0.06}$	$10.00^{+4.00}_{-4.00}$	4, 4, 4
A370.....	$6.6^{+0.7}_{-0.5}$	$0.3^{+0.1}_{-0.1}$	3.1 ^b	5, 5, 6
MS 1358.....	$7.48^{+0.30}_{-0.42}$	$0.32^{+0.09}_{-0.09}$	1.93 ^b	7, 8, 6
A1995.....	$8.59^{+0.86}_{-0.67}$	$0.14^{+0.07}_{-0.07}$	$5.0^{+1.6}_{-1.6}$	9, 9, 9
A611.....	$6.6^{+0.6}_{-0.6}$	0.20 ^c	4.99 ^b	10, ..., 6
A697.....	$9.8^{+0.7}_{-0.7}$	0.20 ^c	3.41 ^b	10, ..., 6
A1835.....	$8.21^{+0.19}_{-0.17}$	$0.35^{+0.04}_{-0.03}$	2.32 ^b	7, 8, 6
A2261.....	$8.82^{+0.37}_{-0.32}$	$0.32^{+0.06}_{-0.05}$	3.28 ^b	7, 8, 6
A773.....	$9.29^{+0.41}_{-0.36}$	$0.21^{+0.05}_{-0.05}$	1.44 ^b	7, 8, 6
A2163.....	$12.2^{+1.1}_{-0.7}$	$0.40^{+0.09}_{-0.08}$	$16.50^{+0.90}_{-1.14}$	11, 12, 12
A520.....	$8.33^{+0.46}_{-0.40}$	$0.14^{+0.06}_{-0.06}$	7.80 ^b	7, 8, 6
A1689.....	$9.66^{+0.22}_{-0.20}$	$0.29^{+0.03}_{-0.03}$	1.82 ^b	7, 8, 6
A665.....	$9.03^{+0.35}_{-0.31}$	$0.22^{+0.04}_{-0.05}$	4.24 ^b	7, 8, 6
A2218.....	$7.05^{+0.22}_{-0.21}$	$0.18^{+0.04}_{-0.04}$	3.24 ^b	7, 8, 6
A1413.....	$7.54^{+0.17}_{-0.16}$	$0.28^{+0.03}_{-0.03}$	2.19 ^b	7, 8, 6

NOTE.—Uncertainties are 68% confidence.

^a Adopted value (see Donahue et al. 1999) and adopted 50% uncertainty.

^b Galactic value (Dickey & Lockman 1990) with adopted 50% uncertainty.

^c Adopted value with assumed 100% uncertainty.

REFERENCES.—(1) Donahue et al. 1999. (2) Donahue 1996. (3) Hughes & Birkinshaw 1998. (4) Schindler et al. 1997. (5) Ota, Mitsuda, & Fukazawa 1998. (6) Dickey & Lockman 1990. (7) Allen & Fabian 1998a. (8) Allen & Fabian 1998b. (9) Patel et al. 2000. (10) J. P. Hughes 2001, private communication. (11) Markevitch et al. 1996. (12) Elbaz, Arnaud, & Böhringer 1995.

the X-ray cooling functions and the conversion factor between detector counts and cgs units, Σ (see § 3.2.4 for details). The cooling functions and conversion factors are summarized in Table 6.

3.2.4. X-Ray Cooling Function

The X-ray cooling function enters the distance calculation linearly and indirectly as the conversion between detector counts and cgs units (see § 4.1). We use a Raymond-Smith (1977) spectrum to describe the hot ICM, which includes contributions from electron-ion thermal bremsstrahlung, line emission, recombination, and two photon processes. We replace the nonrelativistic bremsstrahlung calculation in the Raymond-Smith model with the relativistic calculation of Gould (1980). A discussion of this calculation appears in Reese et al. (2000).

The cooling function results for the *ROSAT* data used in our analysis are summarized in Table 6, where Λ_{eH0} is the cooling function in cgs units, $\Lambda_{eH0}^{\text{det}}$ is the cooling function in detector units, Σ is the conversion between counts and cgs units, and Λ_{bol} is the bolometric cooling function. The cooling functions with relativistic corrections are typically 1.05 times the Raymond-Smith “uncorrected” value for the clusters in our sample.

4. METHOD

4.1. Angular Diameter Distance Calculation

The calculation begins by constructing a model for the cluster gas distribution. We use a spherical isothermal β model to describe the ICM. With this model, the cluster’s extent along the line of sight is the same as that in the plane

of the sky. This is clearly invalid in the presence of cluster asphericities. Thus, cluster geometry introduces an important uncertainty in SZE- and X-ray-derived distances. In general, clusters are dynamically young, are aspherical, and rarely exhibit projected gas distributions that are circular on the sky (Mohr et al. 1995). We currently cannot disentangle the complicated cluster structure and projection effects, but numerical simulations provide a good base for understanding these difficulties. The effects of asphericity contribute significantly to the distance uncertainty for each cluster but are not believed to result in any significant bias in the Hubble parameter derived from a large sample of clusters (Sulkanen 1999).

The spherical isothermal β model has the form (Cavaliere & Fusco-Femiano 1976, 1978)

$$n_e(r) = n_{e0} \left(1 + \frac{r^2}{r_c^2} \right)^{-3\beta/2}, \quad (1)$$

where n_e is the electron number density, r is the radius from the center of the cluster, r_c is the core radius of the ICM, and β is the power-law index. With this model, the SZE signal is

$$\begin{aligned} \Delta T &= f_{(x,T_e)} T_{\text{CMB}} D_A \int d\zeta \sigma_T n_e \frac{k_B T_e}{m_e c^2} \\ &= \Delta T_0 \left(1 + \frac{\theta^2}{\theta_c^2} \right)^{(1-3\beta)/2}, \end{aligned} \quad (2)$$

where ΔT is the thermodynamic SZE temperature decrement/increment, $f_{(x,T_e)}$ is the frequency dependence of the SZE with $x = h\nu/kT_{\text{CMB}}$, $T_{\text{CMB}} (=2.728 \text{ K}; \text{Fixsen et al.}$

TABLE 6
X-RAY COOLING FUNCTIONS

CLUSTER	PSPC				HRI			
	$\Lambda_{\text{eH0}}^{\text{a}}$ ($\times 10^{-24}$ ergs $\text{s}^{-1} \text{cm}^{-3}$)	$\Lambda_{\text{eH0}}^{\text{det b}}$ ($\times 10^{-13}$ counts $\text{s}^{-1} \text{cm}^5$)	Σ^{c} [$\times 10^{-11}$ ergs $\text{s}^{-1} \text{cm}^{-2}$ (counts s^{-1}) $^{-1}$]	Σ^{c} (counts $\text{s}^{-1} \text{cm}^{-2}$ (counts s^{-1}) $^{-1}$)]	$\Lambda_{\text{eH0}}^{\text{det b}}$ ($\times 10^{-13}$ counts $\text{s}^{-1} \text{cm}^5$)	Σ^{c} [$\times 10^{-11}$ ergs $\text{s}^{-1} \text{cm}^{-2}$ (counts s^{-1}) $^{-1}$]	$n_{\text{e}}/n_{\text{H}} = \mu_{\text{H}}/\mu_{\text{e}}$	$\Lambda_{\text{bol}}^{\text{d}}$ ($\times 10^{-23}$ ergs $\text{s}^{-1} \text{cm}^{-3}$)
MS 1137	7.751	1.765	2.461	1.202	2.146
MS 0451	6.948	3.263	1.373	1.373	1.470	3.050	1.198	2.702
Cl 0016	6.922	3.003	1.489	1.489	1.289	3.471	1.197	2.260
R1347	6.922	1.167	4.089	1.201	2.643
A370	6.790	1.627	3.037	1.200	2.223
MS 1358	6.717	3.785	1.336	1.336	1.793	2.821	1.200	2.371
A1995	6.434	1.434	3.395	1.198	2.448
A611	6.511	1.489	3.395	1.199	2.175
A697	6.334	1.570	3.148	1.199	2.647
A1835	6.462	3.839	1.344	1.344	1.775	2.909	1.201	2.496
A2261	6.359	1.649	3.150	1.200	2.570
A773	6.171	1.870	2.715	1.199	2.581
A2163	6.135	2.555	1.998	1.998	1.021	5.000	1.202	3.064
A520	6.119	3.209	1.586	1.586	1.337	3.807	1.198	2.411
A1689	6.158	3.899	1.335	1.335	1.835	2.836	1.200	2.673
A665	6.102	3.616	1.428	1.428	1.570	3.289	1.199	2.550
A2218	6.112	3.789	1.378	1.378	1.691	3.086	1.198	2.237
A1413	6.133	4.000	1.343	1.343	1.856	2.894	1.200	2.361

^a The emissivity in the cluster frame integrated over the *ROSAT* band (0.5–2.0 keV) redshifted to the cluster frame.

^b The emissivity in the detector frame accounting for the response of the instrument.

^c The conversion of detector units to egs units including the $(1+z)$ factor between energy and counts.

^d The bolometric emissivity.

1996) is the temperature of the CMB radiation, k_B is the Boltzmann constant, σ_T is the Thompson cross section, m_e is the mass of the electron, c is the speed of light, ΔT_0 is the central thermodynamic SZE temperature decrement/increment, θ is the angular radius in the plane of the sky and θ_c the corresponding angular core radius, and the integration is along the line of sight $l = D_A \zeta$. The frequency dependence of the thermal SZE is

$$f_{(x, T_e)} = \left(x \frac{e^x + 1}{e^x - 1} - 4 \right) [1 + \delta_{\text{SZE}}(x, T_e)], \quad (3)$$

where $\delta_{\text{SZE}}(x, T_e)$ is the relativistic correction to the frequency dependence. In the nonrelativistic and RJ limits, $f_{(x, T_e)} \rightarrow -2$. We apply the relativistic corrections $\delta_{\text{SZE}}(x, T_e)$ to fifth order in $kT_e/m_e c^2$ (Itoh, Kohyama, & Nozawa 1998), which agrees with other works (Rephaeli 1995; Rephaeli & Yankovitch 1997; Stebbins 1997; Challinor & Lasenby 1998; Sazonov & Sunyaev 1998a, 1998b; Molnar & Birkinshaw 1999; Dolgov et al. 2001) for clusters with $k_B T_e \leq 15$ keV, satisfied by all the clusters in our sample. This correction decreases the magnitude of $f_{(x, T_e)}$ by $\lesssim 5\%$ (typically 3%) for the clusters considered here.

The X-ray surface brightness is

$$S_X = \frac{1}{4\pi(1+z)^4} D_A \int d\zeta n_e n_H \Lambda_{eH} = S_{X0} \left(1 + \frac{\theta^2}{\theta_c^2} \right)^{(1-6\beta)/2}, \quad (4)$$

where S_X is the X-ray surface brightness in cgs units ($\text{ergs s}^{-1} \text{cm}^{-2} \text{arcmin}^{-2}$), z is the redshift of the cluster, n_H is the hydrogen number density of the ICM, $\Lambda_{eH} = \Lambda_{eH}(T_e, \text{abundance})$ is the X-ray cooling function of the ICM in the cluster rest frame in cgs units ($\text{ergs cm}^3 \text{s}^{-1}$) integrated over the redshifted *ROSAT* band, and S_{X0} is the X-ray surface brightness in cgs units at the center of the cluster. Since the X-ray observations are in instrument counts, we also need the conversion factor between detector counts and cgs units, Σ ($S_{X0} = S_{X0}^{\text{det}} \Sigma$), discussed in detail in Reese et al. (2000) along with a description of the calculation of Λ_{eH} , which includes relativistic corrections (Gould 1980) to the Raymond & Smith (1977) spectrum. The normalizations, ΔT_0 and S_{X0} , used in the fit include all of the physical parameters and geometric terms that come from the integration of the β model along the line of sight.

One can solve for the angular diameter distance by eliminating n_{e0} (noting that $n_H = n_e \mu_e / \mu_H$, where $n_j \equiv \rho / \mu_j m_p$ for species j), yielding

$$D_A = \frac{(\Delta T_0)^2}{S_{X0}} \left(\frac{m_e c^2}{k_B T_{e0}} \right)^2 \frac{\Lambda_{eH0} \mu_e / \mu_H}{4\pi f_{(x, T_e)}^2 T_{\text{CMB}}^2 \sigma_T^2 (1+z)^4 \theta_c} \times \left[\frac{\Gamma(3\beta/2)}{\Gamma(3\beta/2 - 1/2)} \right]^2 \frac{\Gamma(3\beta - 1/2)}{\Gamma(3\beta)}, \quad (5)$$

where $\Gamma(x)$ is the gamma function. Similarly, one can eliminate D_A instead and solve for the central density n_{e0} .

More generally, the angular diameter distance is

$$D_A = \frac{(\Delta T_0)^2}{S_{X0}} \left(\frac{m_e c^2}{k_B T_{e0}} \right)^2 \frac{\Lambda_{eH0} \mu_e / \mu_H}{4\pi f_{(x, T_e)}^2 T_{\text{CMB}}^2 \sigma_T^2 (1+z)^4} \times \frac{1}{\theta_c} \frac{\int (n_e/n_{e0})^2 (\Lambda_{eH}/\Lambda_{eH0}) d\eta|_{R=0}}{[\int (n_e/n_{e0}) (T_e/T_{e0}) d\eta|_{R=0}]^2}, \quad (6)$$

where θ_c is the characteristic angular scale of the galaxy cluster whose exact meaning depends on the ICM model (the core radius for the isothermal β model) and $\eta \equiv \zeta/\theta_c \equiv l/r_c$ is the line-of-sight length in units of the characteristic radius, $r_c = \theta_c D_A$. For simplicity in notation, we have assumed that the density and temperature models are normalized at the central value (denoted with 0) although any location for the normalization is allowed. The above integrals are along the central line of sight, denoted as zero projected radius $R = 0$. The Γ functions and the factor of $\pi^{1/2}$ in equation (5) come from the integration of the β model along the central line of sight for both the SZE and X-ray models.

4.2. Joint SZE and X-Ray Model Fitting

The SZE emission and X-ray emission both depend on the properties of the ICM, so a joint fit to the interferometric SZE data and the PSPC and HRI X-ray data provides the best constraints on those properties. Each data set is assigned a collection of parameterized models. Typically, SZE data sets are assigned a β model and point sources and X-ray images are assigned a β model and a cosmic X-ray background model. This set of models is combined for each data set to create a composite model that is then compared to the data.

Our analysis procedure is described in detail in Reese et al. (2000). The philosophy behind the analysis is to keep the data in a reduced but “raw” state and run the model through the observing strategy to compare directly with the data. In particular, the interferometric SZE observations provide constraints in the Fourier u - v plane, so we perform our model fitting in the u - v plane, where the noise properties of the data and the spatial filtering of the interferometer are well defined. The SZE model is generated in the image plane, multiplied by the primary beam, and fast Fourier transformed to produce model visibilities. We then interpolate the model visibilities to the u and v of each data visibility and compute the Gaussian likelihood. For X-ray data, the model is convolved with the appropriate PSF and the Poisson likelihood is computed pixel by pixel, ignoring the masked point-source regions.

Each data set is independent, and likelihoods from each data set can simply be multiplied together to construct the joint likelihood. Likelihood ratio tests can then be performed to get confidence regions or compare two models. Rather than working directly with likelihoods, \mathcal{L} , we work with $S \equiv -2 \ln(\mathcal{L})$. We then construct a $\Delta\chi^2$ -like statistic from the log likelihoods, $\Delta S \equiv S_n - S_{\min}$, where S_{\min} is the minimum of the S function and S_n is the S statistic where n parameters differ from the parameters at S_{\min} . The statistic ΔS is sometimes referred to as the Cash (1979) statistic and tends to a χ^2 distribution with n degrees of freedom for large n (e.g., Kendall & Stuart 1979). This ΔS statistic is equivalent to the likelihood ratio test and is used to generate confidence regions and confidence intervals. For one interesting parameter, the 68.3% ($\sim 1 \sigma$) confidence level corresponds to $\Delta S = 1.0$.

4.2.1. Model Fitting Uncertainty Estimation

Uncertainties in the angular diameter distance from the fit parameters are calculated by varying the interesting parameters to explore the ΔS likelihood space. The most important parameters in this calculation are ΔT_0 , S_{X0} , β ,

and θ_c . Radio point sources and the cosmic X-ray background affect ΔT_0 and S_{X0} , respectively. As a compromise between precision and computation time, we systematically vary ΔT_0 , S_{X0} , β , and θ_c allowing the X-ray backgrounds for the PSPC and HRI to float independently while fixing the positions of the cluster (both SZE and X-ray) and the positions and flux densities of any radio point sources in the SZE cluster fields. We describe our estimation of the effects of point sources below.

From this four-dimensional ΔS hypersurface, we construct confidence intervals for each parameter individually as well as confidence intervals for D_A due to S_{X0} , ΔT_0 , β , and θ_c jointly. To compute the 68.3% confidence region, we find the minimum and maximum values of the parameter within a ΔS of 1.0. We emphasize that these uncertainties are meaningful only within the context of the spherical isothermal β model.

4.2.2. Measured Radio Point Sources

Two methods of estimating the effect of the measured radio point sources in the cluster field are examined, one that is reasonably quick and one that is more rigorous. For the quick estimate, we first determine the 1σ confidence limits on the flux density of each point source by varying the point-source flux density while keeping the ICM parameters fixed at their best-fit values. These are the uncertainties listed in Table 3, after correcting for the primary beam attenuation appropriate for each point source's distance from the pointing center. We then determine the change in the central decrement over the 68.3% confidence region for the point-source flux densities by fixing the point-source flux density at the $\pm 1\sigma$ values and varying ΔT_0 while fixing the ICM shape parameters at their best-fit values. This is done for each point source in the field and all combinations of the $\pm 1\sigma$ flux densities for fields with multiple point sources. We adopt the maximum percentage change in ΔT_0 as our uncertainty from radio point sources on the central decrement. The above procedure will be referred to as the quick estimate of the effects of measured radio point sources. We tested this estimate against marginalizing over the point-source flux density by varying θ_c , β , S_{X0} , ΔT_0 , and point-source flux for each point source, while fixing the X-ray background (which simply saves computation time by isolating the point-source flux issue). From the marginalized likelihood function we find the best fit and 68.3% uncertainty on ΔT_0 and D_A . The uncertainty from measured radio point sources, σ_{pt} , is computed assuming that the uncertainties add in quadrature from

$$\sigma_{pt}^2 = \sigma_{mar}^2 - \sigma_{fix}^2, \quad (7)$$

where σ_{mar} and σ_{fix} are the uncertainties from the marginalized grids and the initial, point-source fixed grids, respectively. Marginalizing over point-source flux density was performed on two clusters with one point source each, A2261 and MS 1358, and one cluster with two point sources, A1835. The quick estimation of the effects of point sources agrees to within 2% on D_A (1% on ΔT_0) with the marginalized likelihood analysis, just slightly overestimating the uncertainty due to point sources. The marginalization procedure is computationally intensive. Therefore, to save computation time, we use the quick procedure to estimate the effects of detected point sources on the central decrement.

As an additional test, we explore the maximum likelihood parameter space (varying θ_c , β , S_{X0} , and ΔT_0) with the point-source fluxes fixed at the $\pm 1\sigma$ values for our three test case clusters: A2261, MS 1358, and A1835. The effects of point sources on the central decrement from this study agree within a few percent with both the quick and marginalized procedures. This is what was originally done for MS 0451 and Cl 0016 (Reese et al. 2000), which is now shown to give essentially the same result as marginalizing over the point-source flux. For all clusters, we use the updated, quick estimates of the effects of measured point sources.

4.3. Model Fitting Results

We apply the analysis procedure described above to all 18 of our galaxy clusters. The results from our maximum likelihood joint fit to the SZE and X-ray data are summarized in Table 7, which shows the best-fit ICM shape parameters and the uncertainties on each parameter from the model fit.

So far, we have only shown the SZE data in the form of images although the data are recorded as visibilities. Figure 4 shows the SZE $u-v$ radial profiles for Cl 0016 with a series of three panels illustrating the features of such profiles. These profiles are azimuthal averages in the Fourier plane plotted as a function of the radius in the $u-v$ plane, $(u^2 + v^2)^{1/2}$. The data are the points with error bars, and the best-fit β model from the joint SZE and X-ray analysis is the solid line averaged the same way as the data. The point sources are subtracted directly from the visibilities before constructing the $u-v$ radial profiles. All of these panels are shown on the same scale for easy comparison. Also plotted are the residuals in units of the standard deviation, $\Delta V/\sigma = (\text{data} - \text{model})/\sigma$. For a circular cluster at the phase center (coincident with the pointing center), one expects a monotonic real component and a zero imaginary component. Clusters are rarely exactly centered at the phase/pointing center of our observations. Therefore, we shift the phase center to the cluster center before constructing the $u-v$ radial profiles. The phase-shifted radial profiles are shown in the top panels of Figure 4 for both the real (*left*) and imaginary (*right*) components of the complex visibilities. The model provides a good fit to the data for a wide range of spatial frequencies. The middle panels show the $u-v$ radial profile when the phase center is not shifted to the center of the cluster. The off-center cluster introduces corrugation in the Fourier plane modifying the expected real component and introducing a nonzero imaginary component. In addition, asymmetry in the cluster will manifest itself as a nonzero imaginary component. Our model is symmetric and its imaginary component should be identically zero. The attenuation from the primary beam introduces asymmetry, producing a nonzero imaginary component. This is illustrated in the bottom panels of Figure 4 showing the $u-v$ radial profile including the phase center shift but not including the primary beam correction when computing the model. Notice that the model is identically zero, unlike the top panels, where the asymmetry produced by the primary beam on the off-center cluster shows a small imaginary component.

The $u-v$ radial profiles for the real and imaginary components of the complex visibilities for each cluster in our sample are shown in Figure 5. Any point sources in the field are subtracted directly from the visibilities, and the phase center is shifted to the center of the cluster before azimuthally aver-

TABLE 7
ICM PARAMETERS

Cluster	β	θ_c (arcsec)	S_{X0}^{det} (detector) (count s ⁻¹ arcmin ⁻²)	S_{X0} (cgs) (ergs s ⁻¹ cm ⁻² arcmin ⁻²)	ΔT_0 (μ K)	D_A (Mpc)
MS 1137	$0.786^{+0.220}_{-0.120}$	$19.4^{+6.4}_{-4.0}$	$1.80^{+0.30}_{-0.24} \times 10^{-2}$	$4.43^{+0.74}_{-0.59} \times 10^{-13}$	-818^{+98}_{-113}	3179^{+1103}_{-1640}
MS 0451	$0.806^{+0.052}_{-0.043}$	$34.7^{+3.9}_{-3.5}$	$6.96^{+0.63}_{-0.61} \times 10^{-2}$	$9.56^{+0.86}_{-0.84} \times 10^{-13}$	-1431^{+98}_{-93}	1278^{+265}_{-299}
Cl 0016	$0.749^{+0.024}_{-0.018}$	$42.3^{+2.4}_{-2.0}$	$4.14^{+0.15}_{-0.19} \times 10^{-2}$	$6.17^{+0.22}_{-0.28} \times 10^{-13}$	-1242^{+105}_{-105}	2041^{+484}_{-514}
R1347	$0.604^{+0.011}_{-0.012}$	$9.0^{+0.5}_{-0.5}$	$6.70^{+0.39}_{-0.34} \times 10^{-1}$	$2.74^{+0.16}_{-0.14} \times 10^{-11}$	-3950^{+350}_{-350}	1221^{+368}_{-343}
A370	$0.518^{+0.090}_{-0.080}$	$39.5^{+10.5}_{-10.5}$	$8.88^{+1.41}_{-0.99} \times 10^{-3}$	$2.70^{+0.43}_{-0.30} \times 10^{-13}$	-1253^{+218}_{-533}	4352^{+1388}_{-1245}
MS 1358	$0.622^{+0.015}_{-0.015}$	$18.2^{+1.4}_{-1.5}$	$1.27^{+0.11}_{-0.08} \times 10^{-1}$	$1.70^{+0.15}_{-0.11} \times 10^{-12}$	-784^{+90}_{-90}	866^{+248}_{-310}
A1995	$0.770^{+0.117}_{-0.063}$	$38.9^{+6.9}_{-4.3}$	$3.18^{+0.24}_{-0.21} \times 10^{-2}$	$1.08^{+0.08}_{-0.07} \times 10^{-12}$	-1023^{+83}_{-77}	1119^{+247}_{-282}
A611	$0.565^{+0.060}_{-0.040}$	$17.5^{+3.5}_{-3.5}$	$5.91^{+1.06}_{-0.76} \times 10^{-2}$	$2.01^{+0.36}_{-0.26} \times 10^{-12}$	-853^{+120}_{-140}	995^{+325}_{-293}
A697	$0.540^{+0.045}_{-0.035}$	$37.8^{+5.6}_{-4.0}$	$3.24^{+0.22}_{-0.25} \times 10^{-2}$	$1.02^{+0.07}_{-0.08} \times 10^{-12}$	-1410^{+160}_{-180}	998^{+298}_{-250}
A1835	$0.595^{+0.007}_{-0.005}$	$12.2^{+0.6}_{-0.5}$	$1.50^{+0.10}_{-0.07} \times 10^{-0}$	$2.02^{+0.14}_{-0.10} \times 10^{-11}$	-2502^{+150}_{-175}	1027^{+194}_{-198}
A2261	$0.516^{+0.014}_{-0.013}$	$15.7^{+1.2}_{-1.1}$	$1.37^{+0.08}_{-0.08} \times 10^{-1}$	$4.31^{+0.26}_{-0.26} \times 10^{-12}$	-1697^{+200}_{-200}	1049^{+306}_{-272}
A773	$0.597^{+0.064}_{-0.032}$	$45.0^{+7.0}_{-5.0}$	$3.05^{+0.24}_{-0.24} \times 10^{-2}$	$8.28^{+0.65}_{-0.65} \times 10^{-13}$	-1260^{+160}_{-160}	1450^{+361}_{-337}
A2163	$0.674^{+0.011}_{-0.008}$	$87.5^{+2.5}_{-2.0}$	$6.82^{+0.12}_{-0.11} \times 10^{-2}$	$1.36^{+0.03}_{-0.03} \times 10^{-12}$	-1900^{+140}_{-140}	828^{+181}_{-205}
A520	$0.844^{+0.040}_{-0.040}$	$123.3^{+8.0}_{-8.0}$	$2.57^{+0.11}_{-0.11} \times 10^{-2}$	$4.08^{+0.18}_{-0.18} \times 10^{-13}$	-662^{+95}_{-95}	723^{+270}_{-236}
A1689	$0.609^{+0.005}_{-0.005}$	$26.6^{+0.7}_{-0.7}$	$4.50^{+0.13}_{-0.11} \times 10^{-1}$	$6.01^{+0.18}_{-0.15} \times 10^{-12}$	-1729^{+105}_{-120}	688^{+172}_{-163}
A665	$0.615^{+0.006}_{-0.006}$	$71.7^{+1.5}_{-1.5}$	$4.75^{+0.08}_{-0.08} \times 10^{-2}$	$6.78^{+0.13}_{-0.12} \times 10^{-13}$	-728^{+150}_{-150}	466^{+217}_{-179}
A2218	$0.692^{+0.008}_{-0.008}$	$67.5^{+1.5}_{-1.8}$	$5.14^{+0.12}_{-0.10} \times 10^{-2}$	$7.08^{+0.16}_{-0.14} \times 10^{-13}$	-731^{+125}_{-100}	1029^{+339}_{-352}
A1413	$0.639^{+0.009}_{-0.009}$	$47.7^{+2.0}_{-2.0}$	$1.52^{+0.07}_{-0.07} \times 10^{-1}$	$2.04^{+0.09}_{-0.09} \times 10^{-12}$	-856^{+110}_{-110}	573^{+171}_{-151}

aging the real and imaginary components of the complex visibilities. The points with error bars are the data, and the best-fit model from the joint SZE and X-ray analysis is shown as a solid line, averaged the same way as the data. Also shown are the residuals in units of the standard deviation. A simple χ^2 analysis of the SZE u - v radial profiles reveals that the models provide a good fit to the data for every cluster. The real and imaginary components are shown on the same scale for each cluster for easy comparison, although the scale on the residuals may change. The cluster with the most apparent imaginary component, A520, is also the cluster with its best-fit center the farthest away from the pointing center, $\sim 65''$. The primary beam attenuation introduces asymmetry and produces a nonzero imaginary component paralleled in the best-fit model for A520.

Figure 6 shows the X-ray radial surface brightness profiles and the best-fit composite models for each cluster in the sample. Residuals in units of the standard deviation are also plotted, $\Delta S_X/\sigma_{S_X}$. A simple χ^2 analysis of the radial profiles shows that, in general, the models provide a reasonable fit to the data over a large range of angular radii. There are three clusters with residuals $\gtrsim 5\sigma$ in a few of the radial bins, A1835, A665, and A2218. In A1835 the model systematically underpredicts the surface brightness for a few intermediate radial bins. This cluster contains a strong cooling flow (e.g., Peres et al. 1998) but shows no sign of a central emission excess over the best-fit model. The other cooling flow clusters in our sample (see § 6.1) do not exhibit large residuals in the X-ray model fit. Both A665 (Gómez, Hughes, & Birkinshaw 2000; Kaloglyan, Nanni, & Vignato 1990; Geller & Beers 1982) and A2218 (Cannon, Ponman, & Hobbs 1999; Girardi et al. 1997; Markevitch 1997; Kneib et al. 1995) exhibit complicated structure, possibly indicating a recent merger. Although these are the worst cases, the best-fit models for these three clusters still provide reasonable descriptions of the data. The only cluster that shows a marginally significant central X-ray surface brightness excess is A2218, which has not been identified with a cooling flow.

We also note that the cooling flow clusters in our sample do not exhibit the largest residuals.

5. DISTANCES AND THE HUBBLE CONSTANT

We use the results from the maximum likelihood model fitting described in §§ 4.2 and 4.3 to compute the angular diameter distance to each of our 18 galaxy clusters. Table 7 shows the derived angular diameter distances for each galaxy cluster as well as the best-fit ICM shape parameters. The uncertainties on D_A include the entire observational uncertainty budget, which are shown for each cluster in Table 8. The uncertainties in the fitted parameters come from the procedure described in § 4.2.1.

The only other parameter that enters directly into the D_A calculation is T_{e0} . Since $D_A \propto T_{e0}^{-2}$, the uncertainty in D_A due to T_{e0} is listed as twice the fractional uncertainty on T_{e0} . The other parameters, column density and metallicity, as well as T_{e0} , affect the X-ray cooling function. We estimate the uncertainties in D_A due to these parameters by taking their 68.3% ranges and seeing how much they affect the cooling function. The uncertainty on D_A due to observations is dominated by the uncertainty in the electron temperature and the SZE central decrement. Note that changes of factors of 2 in metallicity result in a $\sim 1\%$ effect on D_A .

The column densities measured from the X-ray spectra are different from those from H I surveys (Dickey & Lockman 1990). We use the column densities from X-ray spectral fits when possible since that includes contributions from nonneutral hydrogen and other elements that absorb X-rays. For MS 0451 and Cl 0016, using the survey-derived column densities instead of the fitted values changes the angular diameter distance by roughly $\pm 5\%$ (Reese et al. 2000), which we include as a systematic uncertainty (see § 7).

Figure 7 shows the SZE-determined distances for each cluster as a function of redshift. Also plotted are the theoretical angular diameter distance relations assuming $H_0 = 60$ km s⁻¹ Mpc⁻¹ for three different cosmologies: the currently favored Λ cosmology $\Omega_M = 0.3$, $\Omega_\Lambda = 0.7$ (solid line); an

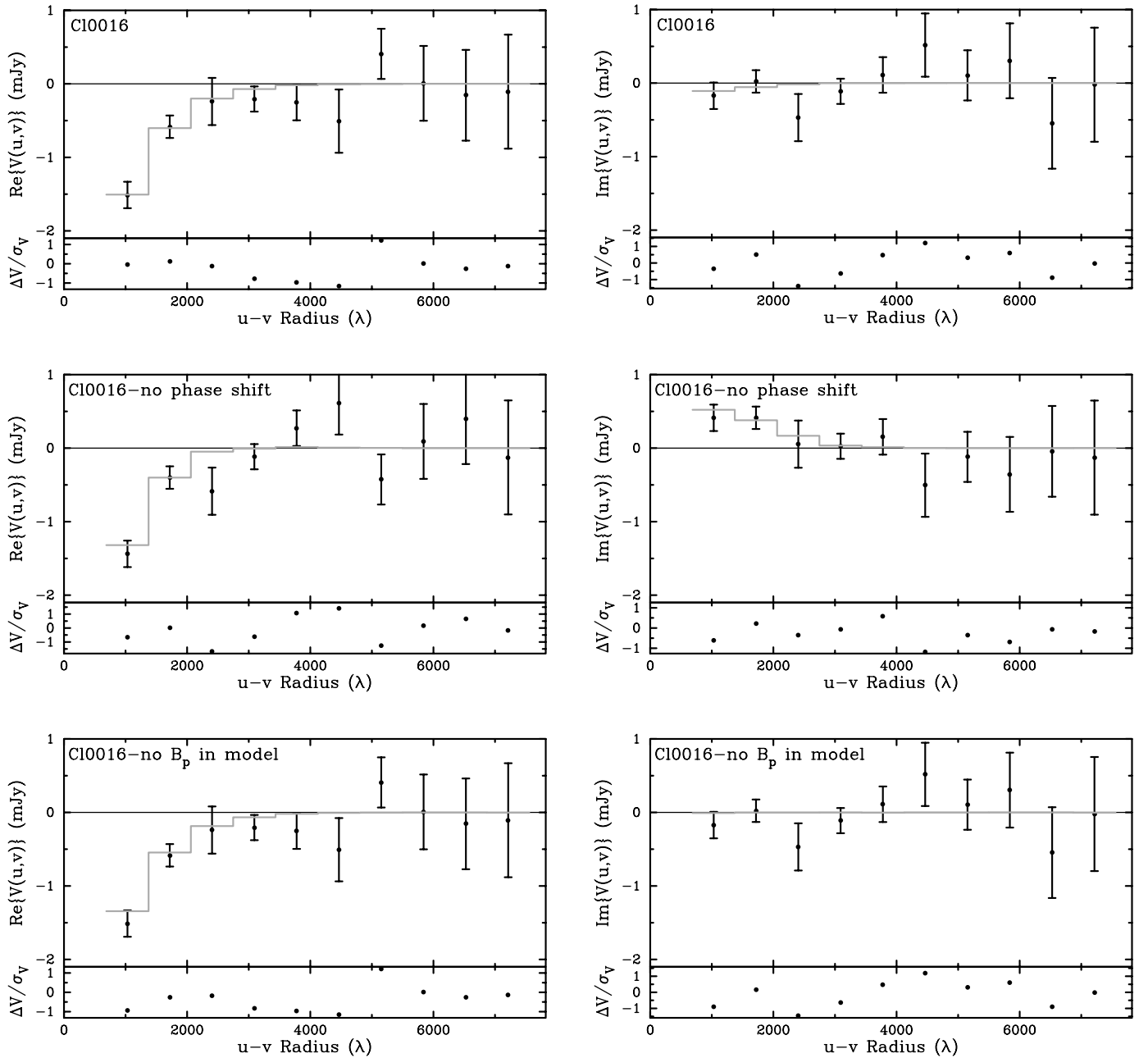


FIG. 4.—Real and imaginary components of the complex visibilities plotted as a function of radius in the u - v plane for Cl 0016. The points with error bars are the data, and the best-fit model from the joint SZE and X-ray analysis is the solid line, averaged the same way as the data. Residuals are shown in units of the standard deviation. Shown are the phase-shifted and primary beam-corrected (*top panel*), not phase-shifted (*middle panel*), and not corrected for primary beam (*bottom panel*) versions. Not shifting the phase center to the center of the cluster (*middle panel*) shows an imaginary component from this offset. Not applying the primary beam attenuation to the model after shifting the phase to the center of the cluster (*bottom panel*) shows the expected zero imaginary component; a real and symmetric image should have a real only Fourier transform. The asymmetry induced by the primary beam correction for the off-center cluster introduces a small imaginary component (see top panel). [See the electronic edition of the *Journal* for a color version of this figure.]

open $\Omega_M = 0.3$ (dashed line) universe; and a flat $\Omega_M = 1$ (dotted line) cosmology. The SZE distances are beginning to probe the angular diameter distance relation. The uncertainties on D_A in Figure 7 are the 68.3% statistical uncertainties only, including all of the statistical uncertainties in the calculation outlined above. We refer the reader to Carroll, Press, & Turner (1992), Kolb & Turner (1990), and Peacock (1999) for derivations of the theoretical angular diameter distance relation.

There is a known correlation between the β and θ_c parameters of the β model. Figure 8 illustrates this corre-

lation and its effect on D_A for MS 1358 and A2261. The filled contours are the 1, 2, and 3 σ ΔS confidence regions for β and θ_c jointly with the plus sign marking the best fit for each cluster. The lines are contours of constant D_A in megaparsecs. With our interferometric SZE data, the contours of constant D_A lie roughly parallel to the β - θ_c correlation, minimizing the effect of this correlation on the uncertainties of D_A . Similar figures for MS 0451 and Cl 0016 appear in Reese et al. (2000), which show similar behavior. The alignment of the D_A contours with the β - θ_c correlation is a general feature of

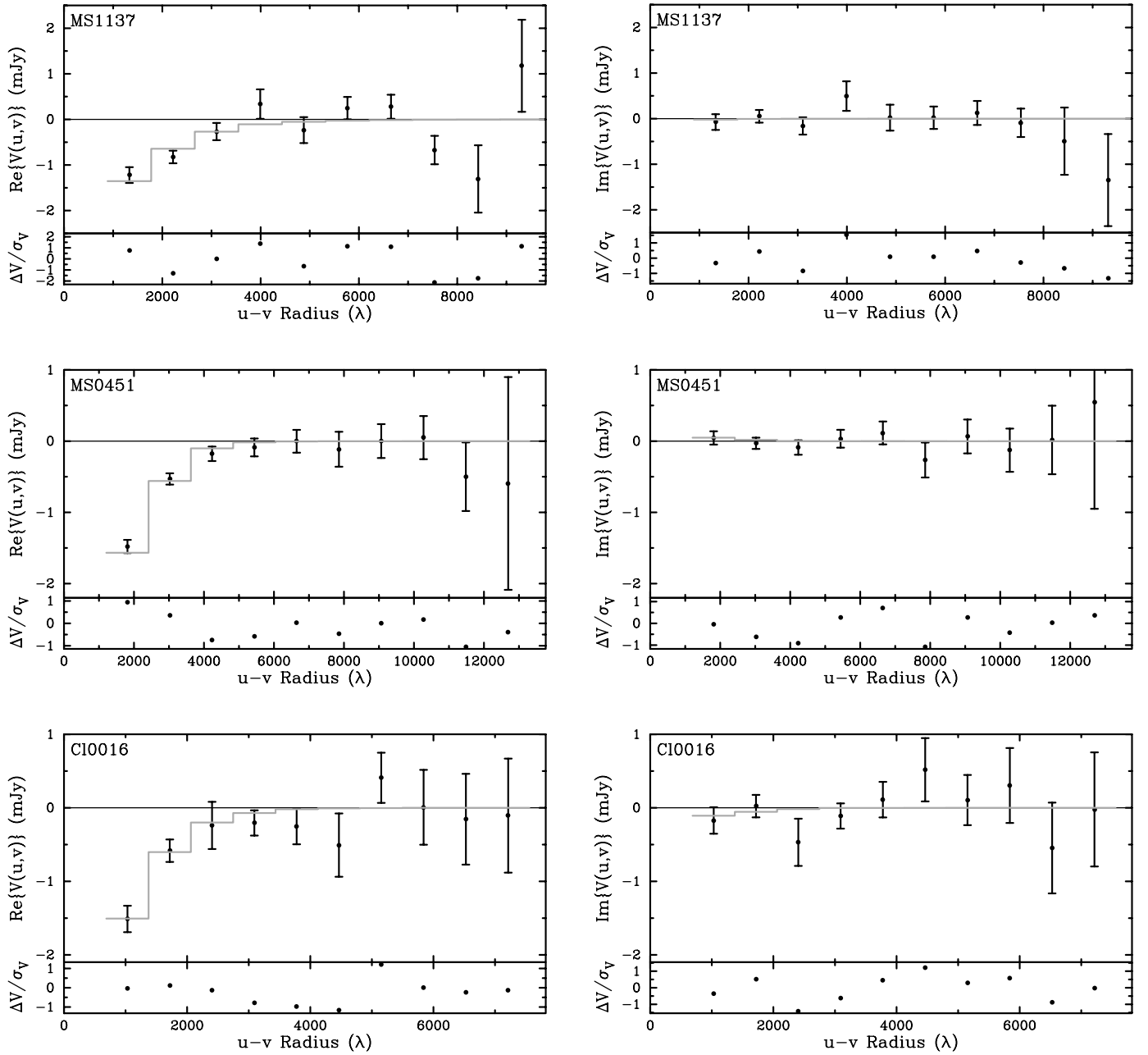


FIG. 5.—Real and imaginary components of the complex visibilities plotted as a function of radius in the u - v plane. The points and error bars are the data, and the solid line is the best-fit model. Residuals are shown in units of the standard deviation. Any point sources in the cluster field have been subtracted directly from the visibilities, and the phase center of the map has been shifted to the center of the cluster before making these radial averages. Nonzero signal in the imaginary components is due to the asymmetry in the cluster and the possible asymmetry introduced by the primary beam correction. The models provide good fits to the data for all the clusters in our sample. [See the electronic edition of the *Journal* for a color version of this figure.]

our observing strategy. Different observing techniques will result in different behavior. Contours of constant D_A have been found to be roughly orthogonal to this β - θ_c correlation for some single-dish SZE observations (Birkinshaw & Hughes 1994; Birkinshaw, Hughes, & Arnaud 1991).

To determine the Hubble constant, we perform a χ^2 fit to our calculated D_A values versus z for three different cosmologies. To estimate statistical uncertainties, we combine the uncertainties on D_A listed in Table 8 in quadrature, which is only strictly valid for Gaussian distributions. This combined statistical uncertainty is symmetrized (averaged) and

used in the fit. We find

$$H_0 = \begin{cases} 60^{+4}_{-4} \text{ km s}^{-1} \text{ Mpc}^{-1}, & \Omega_M = 0.3, \Omega_\Lambda = 0.7, \\ 56^{+4}_{-4} \text{ km s}^{-1} \text{ Mpc}^{-1}, & \Omega_M = 0.3, \Omega_\Lambda = 0.0, \\ 54^{+4}_{-3} \text{ km s}^{-1} \text{ Mpc}^{-1}, & \Omega_M = 1.0, \Omega_\Lambda = 0.0, \end{cases} \quad (8)$$

where the uncertainties are statistical only at 68.3% confidence. The statistical error comes from the χ^2 analysis and includes uncertainties from T_e , the parameter fitting, metallicity, N_H , and detected radio point sources (see Table 8). We have chosen three cosmologies encompassing the

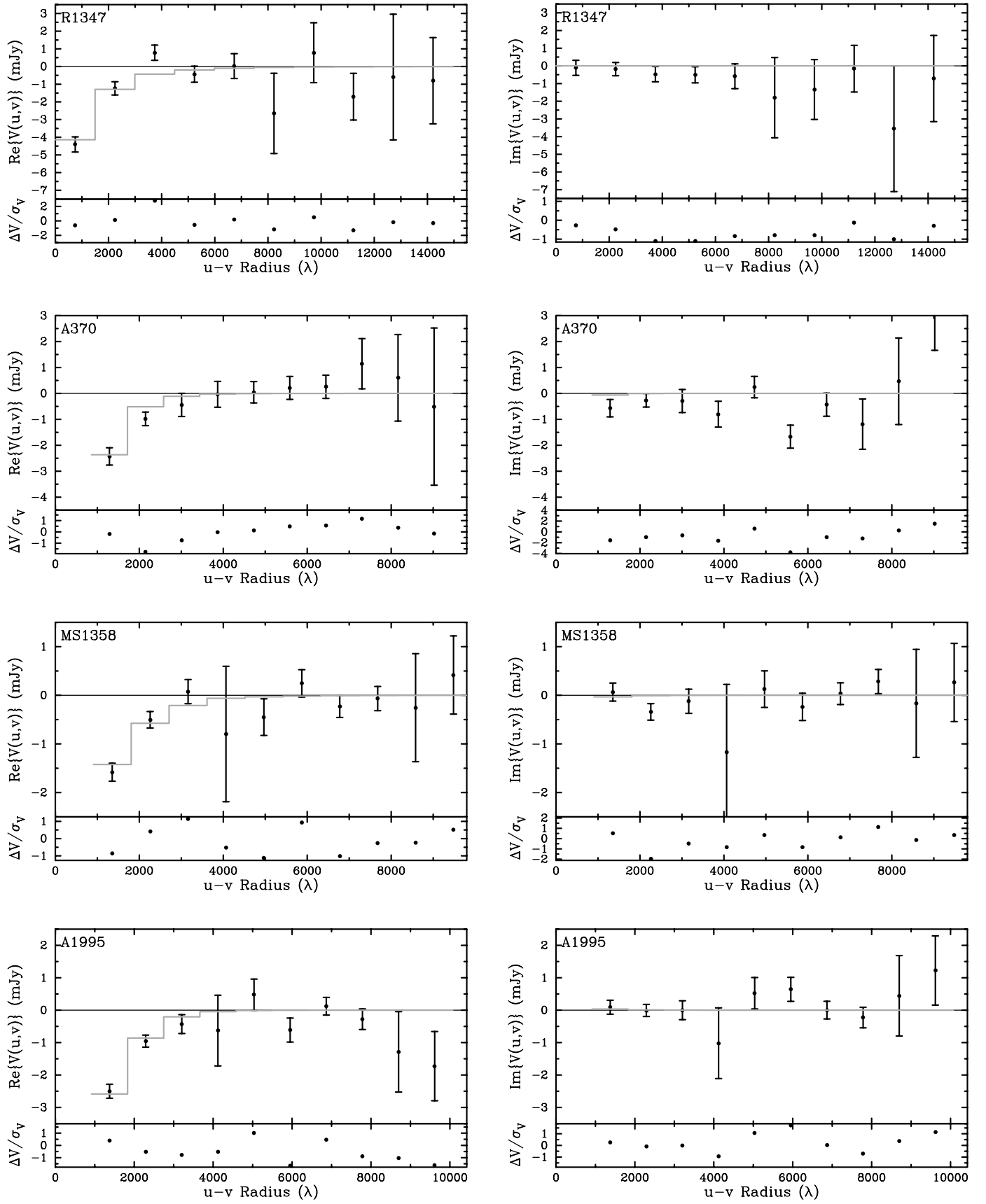


FIG. 5.—*Continued*

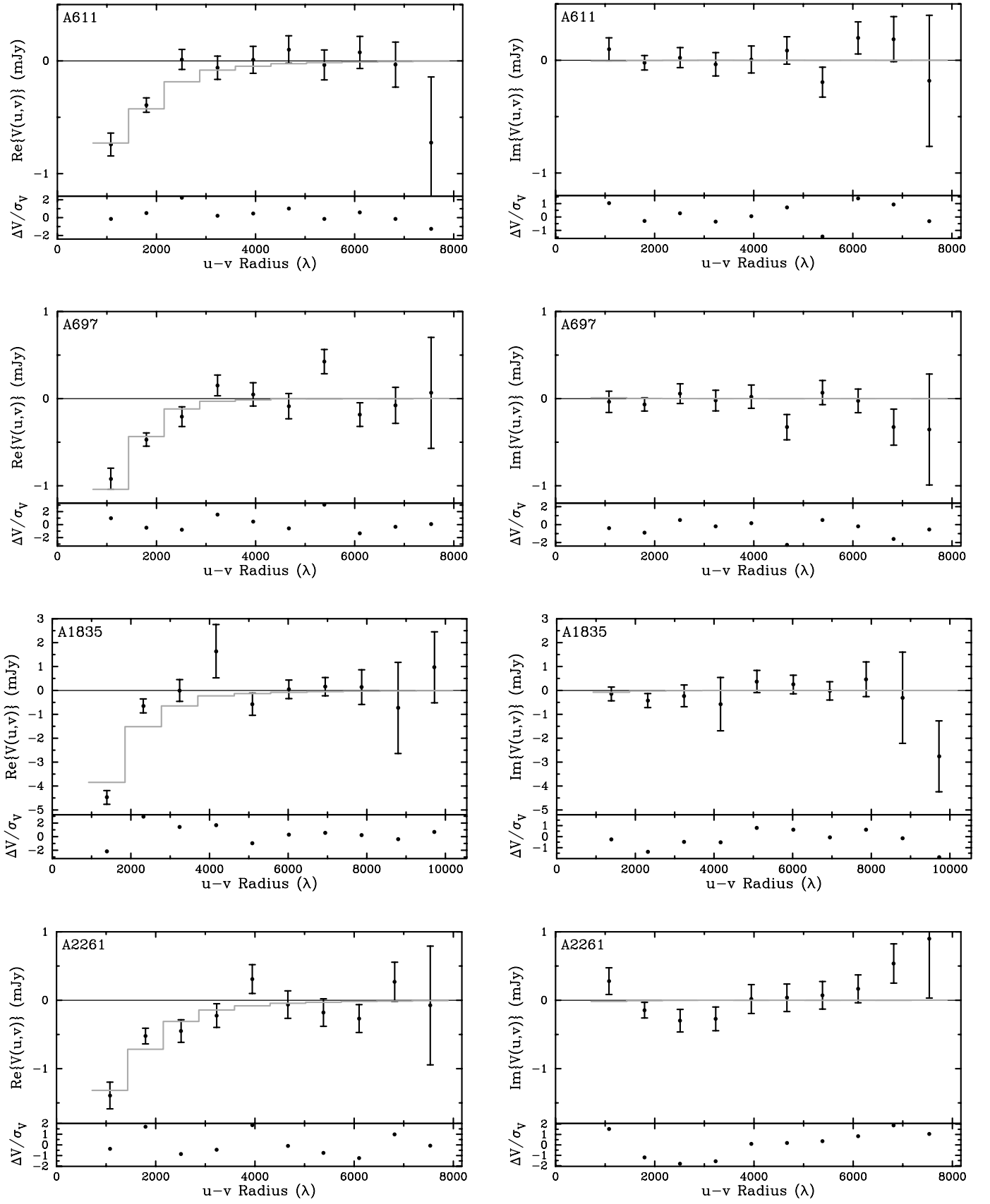


FIG. 5.—*Continued*

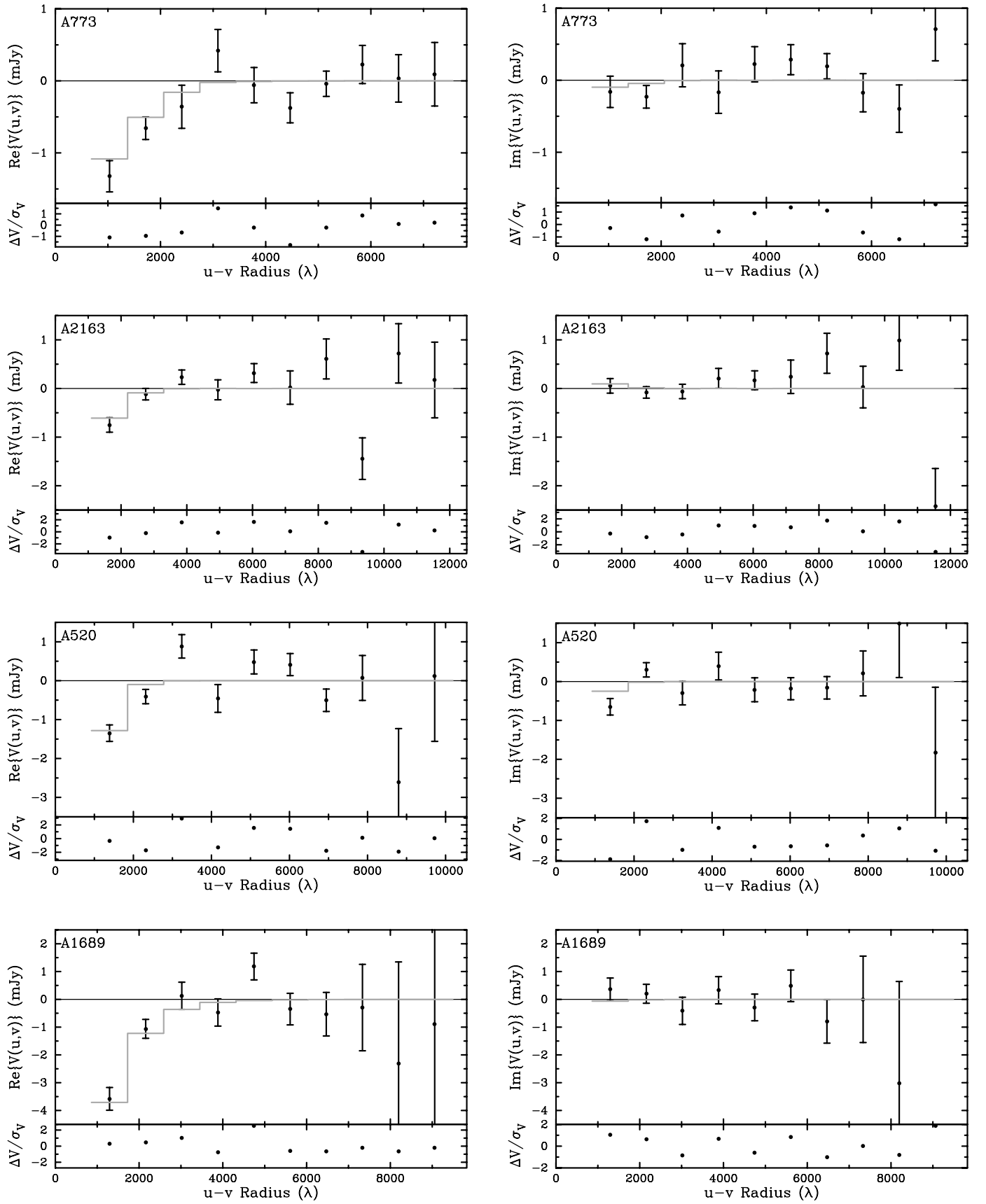
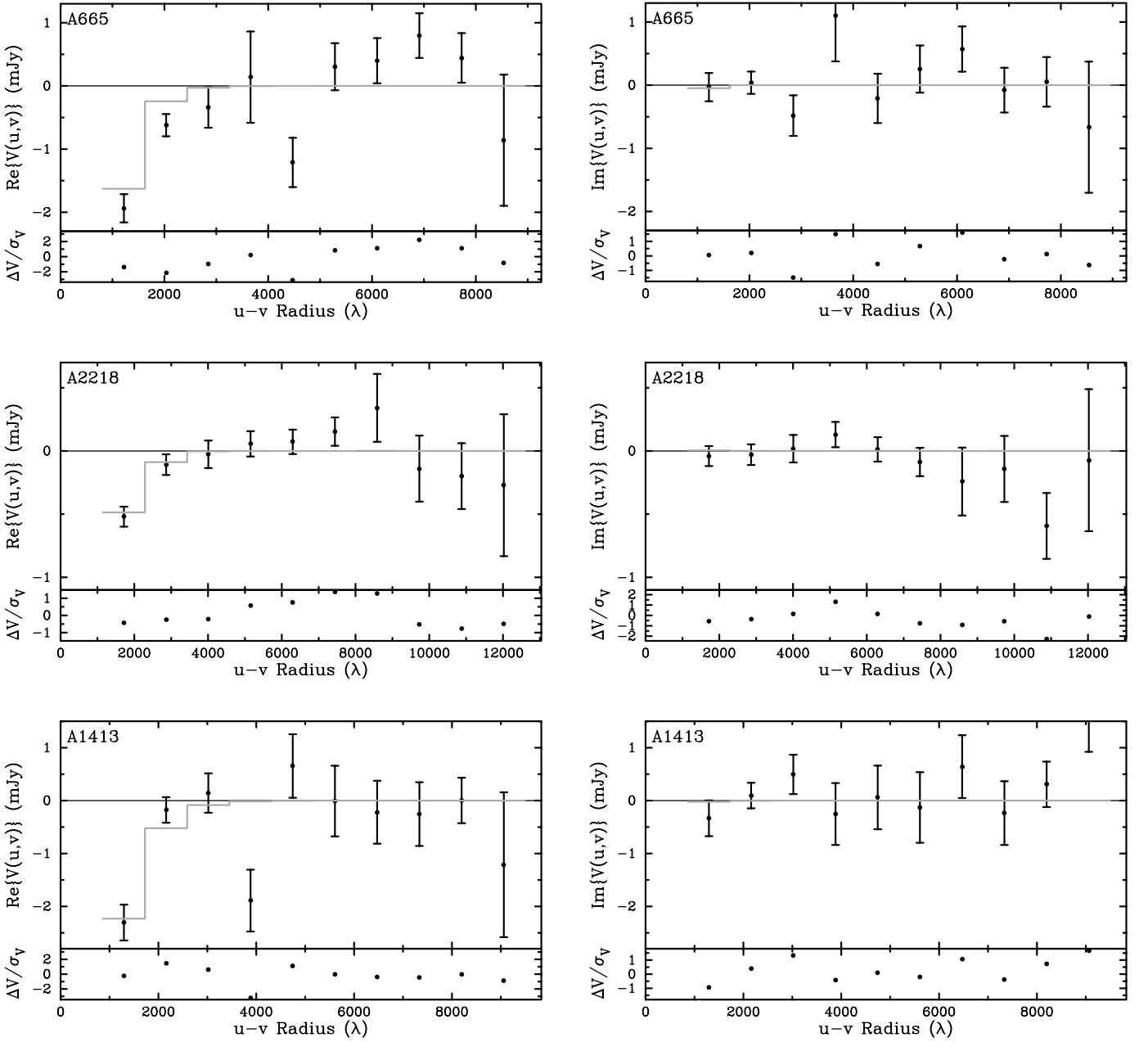


FIG. 5.—Continued

FIG. 5.—*Continued*

currently favored models. With this sample of clusters, there is a $\sim 10\%$ range in our inferred H_0 due to the geometry of the universe. For the Λ cosmology, $\chi^2 = 16.5$ with a corresponding reduced χ^2 of $\chi^2_{\text{red}} = 0.97$. The difference in χ^2 between the $\Omega_M = 0.3$, $\Omega_\Lambda = 0.7$ and the flat $\Omega_M = 1$ universes is roughly $\Delta\chi^2 \sim 0.3$, with the Λ cosmology having the lowest χ^2 . Clearly a larger sample of high-redshift ($z \sim 1$) clusters is required for a determination of the geometry of the universe from SZE- and X-ray-determined direct distances to galaxy clusters (see § 7).

6. SOURCES OF POSSIBLE SYSTEMATIC UNCERTAINTY

The absolute calibration of both the SZE observations and the PSPC and HRI directly affects the distance determinations. The absolute calibration of the interferometric

observations is conservatively known to about 4% at 68.3% confidence, corresponding to an 8% uncertainty in H_0 ($\propto \Delta T_0^{-2}$). The effective areas of the PSPC and HRI are thought to be known to about 10%, introducing a 10% uncertainty into the H_0 determination through the calculation of Σ . In addition to the absolute calibration uncertainty from the observations, there are possible sources of systematic uncertainty that depend on the physical state of the ICM and other sources that can contaminate the cluster SZE emission. Table 9 summarizes the systematic uncertainties in the Hubble constant determined from our 18 cluster sample.

6.1. Cluster Atmospheres and Morphology

6.1.1. Asphericity

Most clusters do not appear circular in radio, X-ray, or optical. Fitting a projected elliptical isothermal β model

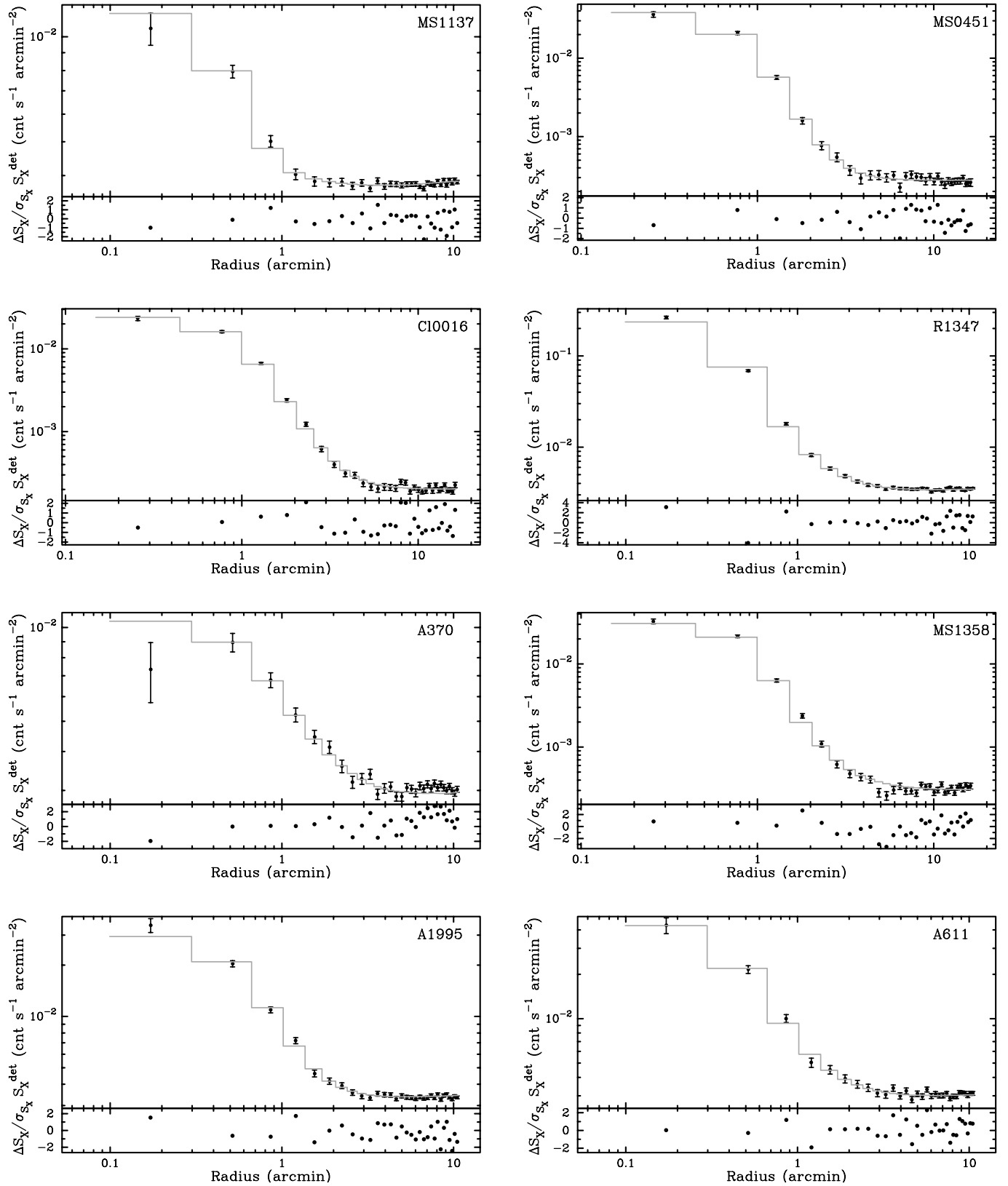
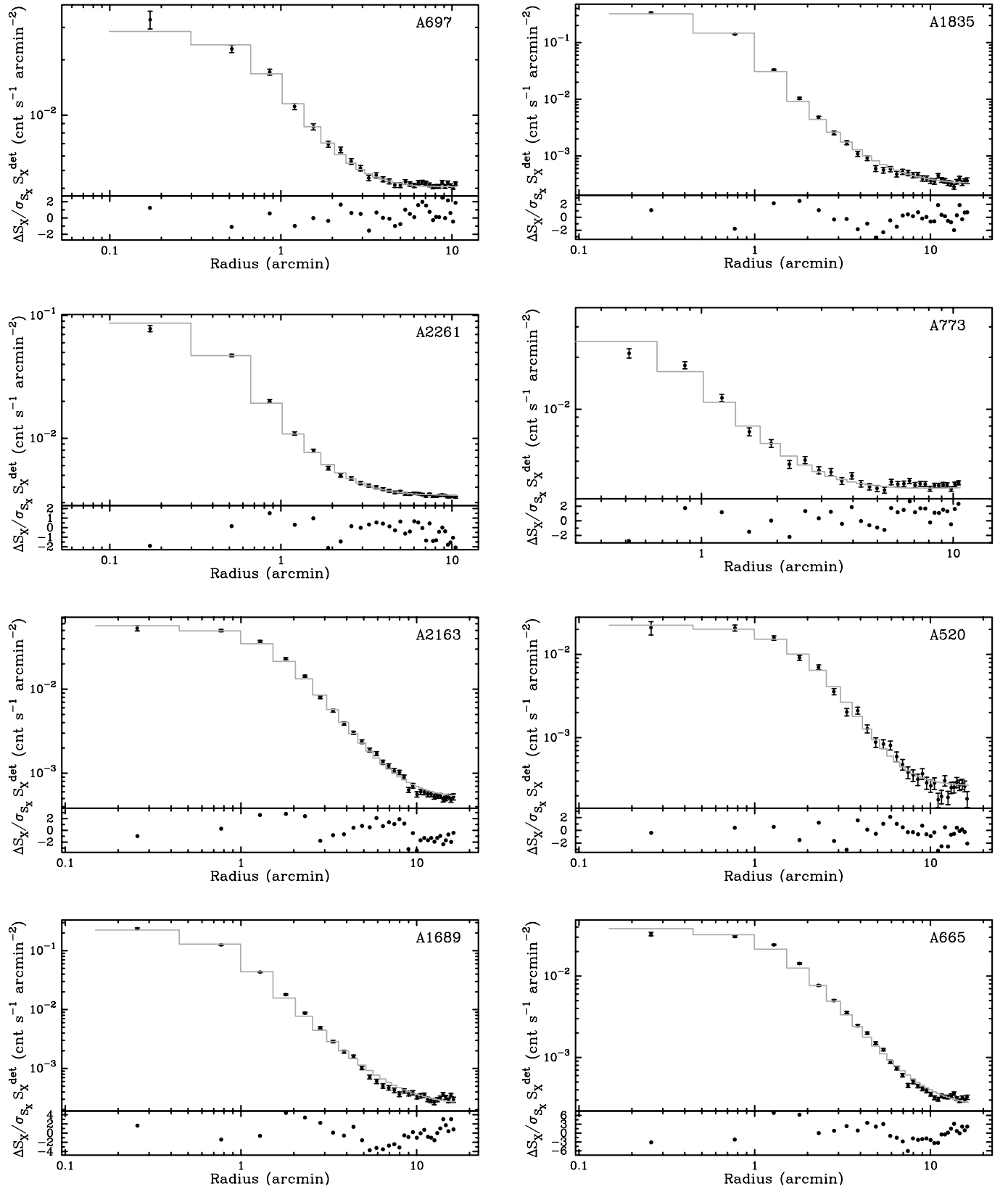


FIG. 6.—X-ray surface brightness radial profiles with the best-fit model and residuals in units of the standard deviation. In general, the models provide good fits to the data over a large range of radii. [See the electronic edition of the *Journal* for a color version of this figure.]

gives typical axial ratios that are close to the local average of 0.80 (Mohr et al. 1995). Under the assumption of axisymmetric clusters, the combined effect of cluster asphericity and its orientation on the sky conspires to introduce a

roughly $\pm 20\%$ random uncertainty in H_0 determined from one galaxy cluster (Hughes & Birkinshaw 1998). When one considers a large, unbiased sample of clusters, with random orientations, the errors due to imposing a spherical model

FIG. 6.—*Continued*

are expected to cancel, resulting in a precise determination of H_0 . Recently, Sulkanen (1999) studied projection effects using triaxial β models. Fitting these with spherical models, he found that the Hubble constant estimated from the sam-

ple was within 5% of the input value. We are in the process of using N -body and smoothed particle hydrodynamics (SPH) simulations of 48 clusters to quantify the effects of complex cluster structure on our results.

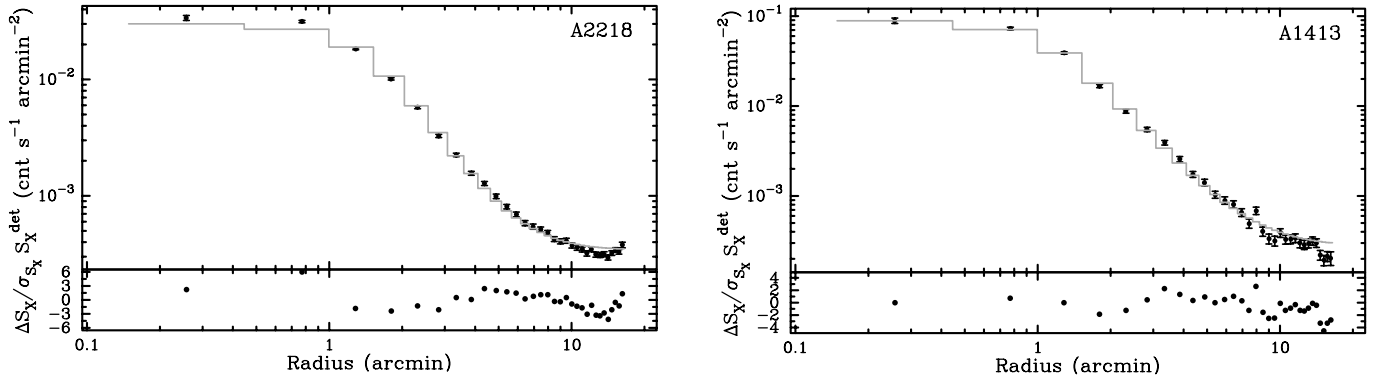


FIG. 6.—Continued

A 20% effect from one cluster implies a 5% $[= 20/\sqrt{18}]$ effect for a sample of 18 clusters. Therefore, we include a 5% effect from asphericity for our cluster sample.

6.1.2. Temperature Gradients

Departures from isothermality in the cluster atmosphere may result in a large error in the distance determination from an isothermal analysis; moreover, an isothermal analysis of a large cluster sample could lead to systematic errors in the derived Hubble parameter if most clusters have similar departures from isothermality (Birkinshaw & Hughes 1994; Inagaki, Sugimotohara, & Suto 1995; Holzapfel et al. 1997b). The *ROSAT* band is fairly insensitive to temperature variations, showing a $\sim 10\%$ change in the PSPC count rate for a factor of 2 change in temperature for $T_e > 1.5$ keV gas (Mohr, Mathiesen, & Evrard 1999). In theory, cluster temperature profiles may significantly affect the distance determinations through the SZE since $\Delta T \propto \int n_e T_e dl$. The spatial filtering of the interferometer

makes our SZE observations insensitive to angular scales larger than a few arcminutes. Therefore, we are relatively insensitive to large-scale temperature gradients. However, we are sensitive to temperature gradients on smaller scales, for example, at the center of cooling flow clusters.

A mixture of simulations and studies of nearby clusters suggests a 10% effect on the Hubble parameter (Inagaki et al. 1995; Roettiger, Stone, & Mushotzky 1997) due to departures from isothermality. The spatial filtering of the interferometer is not accounted for in these studies and thus provides a conservative estimate. We include a conservative $\pm 10\%$ effect on the inferred Hubble parameter due to departures of isothermality, consistent with both cooling flow (see § 6.1.3) and non-cooling flow departures.

6.1.3. Cooling Flows

Cooling flows affect the emission-weighted mean temperature and enhance the X-ray central surface brightness (see, e.g., Fabian 1994; Nagai, Sulkanen, & Evrard 2000). When

TABLE 8
 D_A OBSERVATIONAL UNCERTAINTY BUDGET (%)

Cluster	Fit ^a	T_e^b	$\Lambda_{\text{eff}}(Z)^c$	$\Lambda_{\text{eff}}(N_H)^b$	$\Lambda_{\text{eff}}(T_e)$	Point Source ^d	Total ^e
MS 1137.....	+22.3	+24.6	+4.9	+9.0	+0.0	+0.0	+34.7
	-22.9	-45.6	-4.7	-6.1	-0.8	-0.0	-51.6
MS 0451.....	+13.8	+15.4	+1.0	+0.9	+0.4	+0.6	+20.7
	-13.1	-19.2	-1.0	-1.2	-0.5	-0.6	-23.4
Cl 0016.....	+17.8	+15.4	+1.9	+1.1	+0.1	+1.0	+23.7
	-16.4	-19.1	-1.2	-1.2	-0.2	-0.6	-25.2
R1347.....	+19.2	+12.9	+1.0	+15.7	+0.4	+11.2	+30.1
	-17.1	-15.1	-1.0	-11.7	-0.5	-11.4	-28.1
A370.....	+24.4	+15.2	+1.9	+13.1	+0.4	+4.0	+31.9
	-16.7	-21.2	-1.9	-8.2	-0.6	-4.0	-28.6
MS 1358.....	+24.0	+11.2	+1.5	+3.1	+0.3	+10.0	+28.6
	-21.3	-13.4	-1.5	-3.0	-0.4	-25.2	-35.8
A1995.....	+10.3	+15.6	+1.1	+8.5	+0.5	+8.2	+22.1
	-11.5	-20.0	-1.1	-6.5	-0.7	-7.8	-25.2
A611.....	+22.2	+18.2	+3.7	+15.3	+0.4	+0.0	+32.7
	-20.5	-18.2	-3.7	-9.8	-0.5	-0.0	-29.4
A697.....	+22.7	+14.3	+3.0	+12.9	+0.7	+0.0	+29.9
	-18.7	-14.3	-3.0	-8.2	-0.7	-0.0	-25.1
A1835.....	+13.2	+4.1	+0.7	+3.7	+0.2	+12.4	+18.9
	-12.6	-4.6	-0.5	-3.5	-0.2	-13.4	-19.3
A2261.....	+25.0	+7.3	+0.9	+12.7	+0.4	+3.4	+29.2
	-22.9	-8.4	-0.8	-9.3	-0.5	-3.4	-25.9
A773.....	+21.8	+7.8	+0.7	+9.3	+0.5	+0.0	+24.9
	-20.2	-8.8	-0.7	-6.2	-0.5	-0.0	-22.9
A2163.....	+16.3	+11.5	+1.2	+2.9	+0.7	+8.4	+21.8
	-14.4	-18.0	-1.1	-2.2	-1.0	-8.6	-24.8
A520.....	+32.4	+9.6	+1.0	+12.1	+0.3	+10.2	+37.3
	-27.2	-11.0	-1.0	-10.2	-0.4	-10.2	-32.7
A1689.....	+14.4	+4.1	+0.5	+2.9	+0.2	+19.8	+25.0
	-12.2	-4.6	-0.5	-2.8	-0.2	-19.6	-23.7
A665.....	+45.5	+6.9	+0.6	+6.7	+0.3	+0.4	+46.5
	-37.3	-7.8	-0.8	-6.1	-0.4	-0.6	-38.5
A2218.....	+30.3	+6.0	+0.7	+5.2	+0.2	+10.0	+32.9
	-31.7	-6.2	-0.7	-4.8	-0.2	-10.0	-34.2
A1413.....	+28.5	+4.2	+0.5	+3.5	+0.2	+7.2	+29.9
	-24.8	-4.5	-0.5	-3.3	-0.2	-7.2	-26.4

^a The 68.3% uncertainties over the four-dimensional error surface for β , θ_c , S_{X0} , and ΔT_0 .

^b D_A decreases as parameter increases.

^c Metallicity relative to solar.

^d Maximum effect from detected point sources.

^e Combined in quadrature.

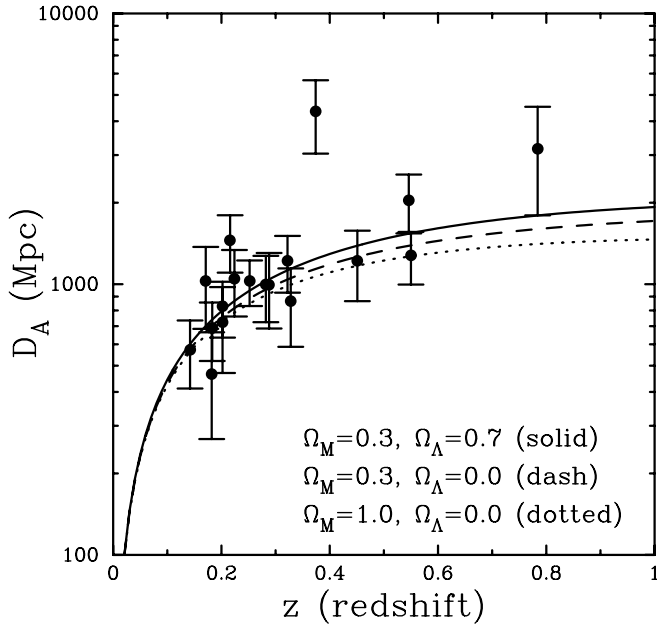


FIG. 7.—SZE-determined distances as a function of redshift. The error bars are 68.3% statistical uncertainties only. Also plotted are the theoretical angular diameter distance relations assuming $H_0 = 60 \text{ km s}^{-1} \text{ Mpc}^{-1}$ for three different cosmological models: the currently favored Λ cosmology $\Omega_M = 0.3$, $\Omega_\Lambda = 0.7$ (solid line); an open $\Omega_M = 0.3$ (dashed line) universe; and a flat $\Omega_M = 1$ (dotted line) cosmology. [See the electronic edition of the *Journal* for a color version of this figure.]

the cooling time at the center of the cluster is less than the age of the cluster, then the central gas has time to cool. This is known as a cooling flow (e.g., Fabian 1994). The cluster temperature is expected to decrease toward the center of the

cluster, which has recently been seen with both *Chandra* (e.g., Markevitch et al. 2000; Nevalainen, Markevitch, & Forman 2000) and *XMM-Newton* (e.g., Tamura et al. 2001).

A characteristic cooling time for the ICM is the available radiative energy divided by its luminosity given by

$$t_{\text{cool}} \sim \frac{3kT_e n_{\text{tot}}}{2\Lambda n_e n_H} = \frac{3kT_e \mu_H}{2\Lambda n_e \mu_{\text{tot}}}, \quad (9)$$

where Λ is the bolometric cooling function of the cluster and all quantities are evaluated at the center of the cluster. Cooling flows may occur if the cooling time is less than the age of the cluster, which we conservatively estimate to be the age of the universe at the redshift of observation, $t_{\text{cool}} < t_H(z)$.

As a check, we calculate t_{cool}/t_H ratios for each cluster analyzed by Mohr et al. (1999). We check our cooling flow and non-cooling flow determinations versus those of Peres et al. (1998) and Fabian (1994). Of the 45 clusters in the Mohr sample, 41 have published mass deposition rates. We assume that the cluster does not contain a cooling flow if its mass deposition rate is consistent with zero; otherwise, it is designated as a cooling flow cluster. We are able to predict whether a cluster has a cooling flow or not with a 90% success rate, suggesting that the ratio t_{cool}/t_H presented in equation (9) is a good predictor for the presence of a cooling flow.

The ratio $t_{\text{cool}}/t_H(z)$ for each cluster is summarized in Table 10 for the same three cosmologies used to determine the Hubble constant. The central densities, n_{e0} , used in this calculation are determined by eliminating D_A in equations (2) and (4) in favor of n_{e0} . From this analysis, the seven clusters R1347, MS 1358, A611, A1835, A2261, A1689, and A1413 are cooling flow clusters. Both A1995 and A1413 are

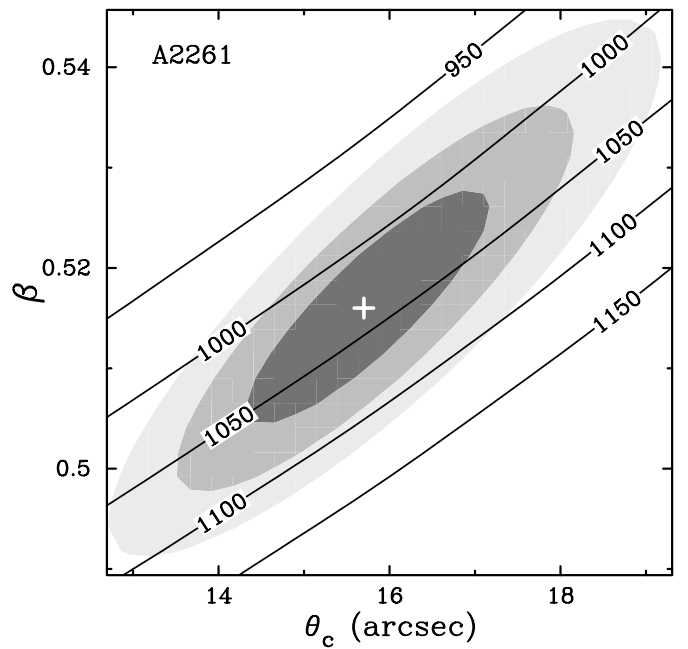
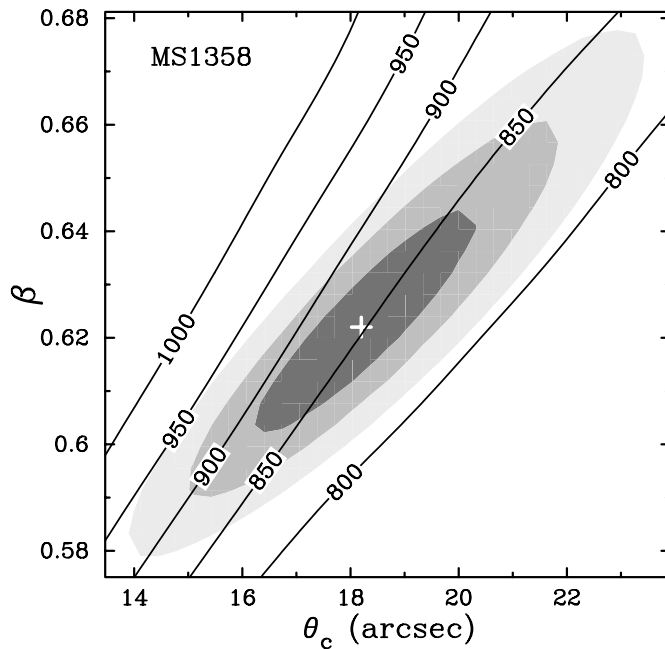


FIG. 8.—Confidence regions from the joint SZE and X-ray fit for MS 1358 and A2261. The filled regions are 1, 2, and 3 σ confidence regions for β and θ_c jointly ($\Delta S = 2.3, 6.2, 11.8$), and the cross marks the best-fit β and θ_c . Solid lines are contours of angular diameter distance in megaparsecs. The D_A contours lie roughly parallel to the β - θ_c correlation, minimizing the effect of this correlation on the uncertainties of D_A . [See the electronic edition of the *Journal* for a color version of this figure.]

TABLE 9
 H_0 SYSTEMATIC UNCERTAINTY BUDGET (%)

Systematic	Effect
SZE calibration.....	± 8
X-ray calibration	± 10
N_H	± 5
Asphericity ^a	± 5
Isothermality	± 10
Clumping	-20
Undetected radio sources ^b	± 12
Kinetic SZE ^a	± 2
Primary CMB ^a	$< \pm 1$
Radio halos	-3
Primary beam	± 3
Total ^c	$+22$ -30

^a Includes a $1/\sqrt{18}$ factor for our 18 cluster sample.

^b Average of effect from the 18 cluster fields.

^c Combined in quadrature.

borderline cases. Such clusters are expected to have falling temperatures toward the center of the cluster.

In principle, the multiphase medium expected in cooling flow clusters could introduce large biases in isothermal β model SZE and X-ray distances (Nagai & Mohr 2002). However, recent observations with *Chandra* and *XMM-Newton* suggest that cooling flows are not as strong as previously expected (e.g., Fabian et al. 2001; Peterson et al. 2001). To estimate the possible effects of cooling flow-like temperature profiles, we adopt the deprojected temperature profile of A1835 from an analysis of *XMM-Newton* observations and determine the change in the angular diameter distance introduced by this profile. The inclusion of the A1835 temperature profile reduces the angular diameter distance by $\sim 10\%$, causing a $\sim 10\%$ underestimate in the Hubble constant from cooling flow clusters when an isothermal analysis is performed (A. D. Miller 2001, private communication). In addition, a theoretical examination of

the effects of cooling flows on SZE- and X-ray-determined distances suggests a $\sim 10\%$ underestimate of H_0 from an isothermal analysis (Majumdar & Nath 2000). Assuming that all seven cooling flow clusters in our sample produce a similar 10% bias in H_0 , the average underestimate in H_0 for our 18 cluster sample is $\sim 4\%$.

We combine the uncertainty from cooling flow and non-cooling flow (see § 6.1.2) departures from isothermality into a conservative $\pm 10\%$ effect on the inferred Hubble parameter.

6.1.4. Clumping and Small-Scale Structure

Clumping of the intracluster gas is a potentially serious source of systematic error in the determination of the Hubble constant. Unresolved clumps in an isothermal intracluster plasma will enhance the X-ray emission by the factor

$$C \equiv \frac{\langle n_e^2 \rangle}{\langle n_e \rangle^2}. \quad (10)$$

The cluster generates more X-ray emission than expected from a uniform ICM, leading to an underestimate of the angular diameter distance ($D_A \propto S_X^{-1}$) and therefore an overestimate of the Hubble parameter for $C > 1$. Unlike the orientation bias, which averages down for a large sample of clusters, clumping must be measured in each cluster or estimated for an average cluster. Theoretical estimates of C are difficult because they must account for the complicated processes that both generate and damp density enhancements, such as preheating and gasdynamical processes.

There is currently no observational evidence of significant clumping in galaxy clusters. If clumping were significant and had large variations from cluster to cluster, we might expect larger scatter than is seen in the Hubble diagrams from SZE and X-ray distances (Fig. 7; see also Birkinshaw 1999). Gasdynamical cluster simulations provide an opportunity to test the effects of observing strategy and cluster structure on our distance determinations. These simulated clusters exhibit X-ray merger signatures consistent with those observed in real clusters, and, presumably, they exhibit the appropriate complexities in their temperature structure as well. Preliminary work indicates that temperature profiles do not introduce a large error on our distances but that clumping in the ICM may bias distances low by up to $\sim 20\%$. As mentioned above, there is no observational evidence of clumping within the ICM. However, merger signatures are common (Mohr et al. 1995), and the mergers are the driving mechanism behind these fluctuations in the simulated clusters (Mathiesen, Evrard, & Mohr 1999).

Clumping causes an overestimate of H_0 , so we include a conservative one-sided -20% possible systematic due to clumping.

6.2. Possible SZE Contaminants

6.2.1. Possible Undetected Point Sources in the Field

Undetected point sources near the cluster center mask the central decrement, causing an underestimate in the magnitude of the decrement and therefore an underestimate of the angular diameter distance. The synthesized beam shapes, which include negative sidelobes, allow both underestimates and overestimates in the magnitude of the decrement. As a conservative estimate of our detection threshold, we use 3 times the rms of the high-resolution map, applying a ≥ 2000

TABLE 10
 RATIO OF $t_{\text{cool}}/t_H(z)$

CLUSTER	COSMOLOGY (Ω_M, Ω_Λ)		
	(0.3, 0.7)	(0.3, 0.0)	(1.0, 0.0)
MS 1137.....	1.1	1.9	1.4
MS 0451.....	1.0	1.6	1.2
Cl 0016.....	1.5	2.5	1.9
R1347.....	0.1	0.2	0.1
A370.....	3.6	5.8	4.4
MS 1358.....	0.4	0.7	0.5
A1995.....	0.9	1.5	1.2
A611.....	0.4	0.7	0.5
A697.....	1.1	1.7	1.3
A1835.....	0.1	0.2	0.2
A2261.....	0.3	0.5	0.4
A773.....	1.5	2.4	1.8
A2163.....	1.3	2.0	1.6
A520.....	2.1	3.3	2.6
A1689.....	0.3	0.5	0.4
A665.....	1.2	1.8	1.4
A2218.....	1.4	2.2	1.7
A1413.....	0.6	0.9	0.7

Å cut on the baselines for each cluster data set. Placing a point source with flux equal to our detection limit near the cluster center and reanalyzing to find the change in the central decrement provides an estimate of the upper bound of the effects of undetected radio point sources.

We have additional information on the distribution of point sources in all our cluster fields from observations at lower frequencies. Sources with flux densities greater than 2 mJy at 1.4 GHz appear in the NVSS catalog (Condon et al. 1998). We use the NVSS catalog to find point sources within $400''$ of each cluster center. We extrapolate the NVSS sources in our fields to 28.5 GHz using the average spectral index of radio sources in galaxy clusters $\alpha = 0.77$ (Cooray et al. 1998), where $S_\nu \propto \nu^{-\alpha}$. Extrapolated NVSS sources with fluxes greater than our 3σ threshold are ruled out by the 30 GHz data, and their fluxes are fixed at the maximal 30 GHz 3σ value. The extrapolated NVSS sources are added to the 30 GHz visibilities data, which are reanalyzed, not accounting for the additional point sources. The uncertainty on the angular diameter distance from undetected point sources is summarized in Table 11 for each cluster field. The average over the 18 cluster fields yields a $\sim 12\%$ uncertainty on the Hubble parameter.

We know that clusters have central dominant (cD) galaxies, which are often radio bright. Therefore, it is likely that there is a radio point source near the center of each cluster. To estimate the effects of cD galaxies on the central decrement, we pick three clusters for which we do not detect a central radio point source, A697, A2261, and A1413. We add a point source fixed at the optical position of the cD (Crawford et al. 1999) and vary both the flux of the cD galaxy and the central decrement, keeping the ICM shape parameters fixed at their best-fit values. The cD fluxes are all consistent with zero, and the corresponding changes in the central decrement are $\lesssim 2\%$. This suggests that undetected cD galaxies do not contribute significantly to the uncertainty on the Hubble constant, $\lesssim 4\%$, within our uncertainty budget for possible undetected point sources.

6.2.2. Kinetic SZE

Cluster peculiar velocities with respect to the CMB introduce an additional CMB spectral distortion known as the kinetic SZE. The kinetic SZE is proportional to the thermal effect but has a different spectral signature so it can be distinguished from the thermal SZE with spectral SZE observations. For a 10 keV cluster with a line-of-sight peculiar velocity of 1000 km s^{-1} , the kinetic SZE is $\sim 11\%$ of the thermal SZE at 30 GHz. Watkins (1997) presented observational evidence suggesting a one-dimensional rms peculiar velocity of $\sim 300 \text{ km s}^{-1}$ for clusters, and recent simulations found similar results (Colberg et al. 2000). With a line-of-sight peculiar velocity of 300 km s^{-1} and a more typical 8 keV cluster, the kinetic SZE is $\sim 4\%$ of the thermal effect, introducing up to a roughly $\pm 8\%$ correction to the angular diameter distance computed from one cluster. When averaged over an ensemble of clusters, the effect from peculiar velocities should cancel, manifesting itself as an additional statistical uncertainty similar to the effects of asphericity. Therefore, we include a $2\% [= 8/\sqrt{18}]$ effect from the kinetic SZE for our 18 cluster sample.

TABLE 11
EFFECTS OF UNDETECTED POINT SOURCES
ON D_A (%)

Cluster	Effect (%)
MS 1137.....	0
MS 0451.....	0
Cl0016.....	2
R1347 ^a	32
A370.....	6
MS 1358 ^b	0
A1995.....	6
A611 ^b	0
A697.....	6
A1835.....	0
A2261 ^a	46
A773.....	6
A2163 ^a	22
A520 ^a	16
A1689 ^a	18
A665 ^a	12
A2218.....	0
A1413.....	42
Average.....	12

^a Required 30 GHz 3σ truncation.

^b No NVSS sources in the cluster field.

6.2.3. CMB Primary Anisotropies

CMB primary anisotropies have the same spectral signature as the kinetic SZE. Recent BIMA observations provide limits on primary anisotropies on the scales of the observations presented here (Dawson et al. 2001; Holzapfel et al. 2000). They place a 95% confidence upper limit to the primary CMB anisotropies of $\Delta T < 19 \mu\text{K}$ at $l \sim 5500$ ($\sim 2'$ scales). Thus, primary CMB anisotropies are an unimportant ($\lesssim 2\%$) source of uncertainty for our observations. At 68.3% confidence, primary CMB anisotropies contribute a $\lesssim 1\%$ uncertainty in the measured Hubble parameter. In addition, CMB primary anisotropy effects on the inferred H_0 should average out over the sample; with an 18 cluster sample CMB primary anisotropy contributes less than 1% uncertainty to H_0 .

6.2.4. Radio Halos

The SZE decrement may be masked by large-scale diffuse nonthermal radio emission in clusters of galaxies, known as radio halos. If present, radio halos are located at the cluster centers, have sizes typical of galaxy clusters, and have a steep radio spectrum $\alpha \sim 1-3$ (Kempner & Sarazin 2001; Giovannini, Tordi, & Feretti 1999; Moffet & Birkinshaw 1989; Hanisch 1982). Similar structures at the cluster periphery, usually with an irregular shape, are called relics. In general, radio halos and relics are rare phenomena that are present in rich, massive clusters, characterized by high X-ray luminosity and high temperature (Giovannini & Feretti 2000; Giovannini et al. 1999). Cooling flow clusters rarely contain radio halos. Because halos and relics are rare, little is known about their nature and origin, but they are thought to be produced by synchrotron emission from an accelerated or reaccelerated population of relativistic electrons (e.g., Jaffe 1977; Dennison 1980; Roland 1981; Schlickeiser, Sievers, & Thiemann 1987). Shocks from

cluster mergers may be the acceleration mechanism, although there are numerous theories (e.g., Jaffe 1977, 1980; Dennison 1980; Roland 1981; Schlickeiser et al. 1987; Ensslin et al. 1998; Blasi & Colafrancesco 1999; Dolag & Ensslin 2000; Liang et al. 2000).

According to the literature (Kempner & Sarazin 2001; Giovannini & Feretti 2000; Giovannini et al. 1999), the following clusters in our sample exhibit radio halos: Cl 0016, A773, A2163, A520, A665, A2218. In Figure 9 we show NVSS 1.4 GHz image contours (Condon et al. 1998) overlaid on gray-scale images of the SZE cluster emission. Contours are multiples of twice the rms in the NVSS maps (rms ~ 0.45 mJy beam $^{-1}$). It is apparent that many of these halos are at the $2\sigma \approx 0.9$ mJy beam $^{-1}$ level. The brightest known halo is seen in A2163 with a peak brightness of ~ 5.4 mJy beam $^{-1}$.

For each of the halo clusters, we conservatively model the halo as a point source at the cluster center with flux from an $\alpha = 1$ extrapolation of the peak NVSS halo flux and reanalyze to determine the effect on the central decrement. The average effect on the central decrement from the clusters with radio halos in our sample is 4%, excluding A2163, which shows a $\sim 10\%$ effect on the central decrement. Radio halos typically have spectral indices $\alpha \geq 1.5$, making the $\alpha = 1$ extrapolation a conservative upper bound for the effects of radio halos. Averaged over the entire 18 cluster sample, the $\alpha = 1$ extrapolation results imply a $\sim 3\%$ overestimate (-3% effect) on our inferred Hubble parameter ($H_0 \propto \Delta T^{-2}$) from radio halos.

6.2.5. Imprecisely Measured Primary Beam

The primary beam is determined from holography measurements at both OVRO and BIMA. The effect of the primary beam on the interferometric observations is a convolution in the Fourier plane (see § 3.1.1) or, equivalently, an attenuation across the field of view. Therefore, differences in primary beam shape simply alter the smoothing kernel in the u - v plane only slightly, having a small effect on the derived distances.

To assess the effects of the primary beam quantitatively, we fit to an OVRO and BIMA data set using a cluster model attenuated by a Gaussian beam with different assumed FWHMs. There is no significant change in the central decrements when using a Gaussian approximation for the primary beam instead of the measured beam. Even with an unrealistically large ± 0.2 uncertainty in the primary beam FWHM, the uncertainty introduced in the Hubble constant is $\lesssim 3\%$ ($\lesssim 2\%$ in ΔT_0). Artificially broadening the wings of the real beam has a negligible effect on the derived central decrements. We adopt a 3% uncertainty in H_0 as a conservative estimate of the maximum effects from an imprecisely measured primary beam.

7. DISCUSSION AND CONCLUSION

We perform a maximum likelihood joint fit to centimeter-wave interferometric SZE and *ROSAT* X-ray (PSPC and HRI) data to constrain the ICM parameters for a sample of high-redshift clusters of galaxies. We model the ICM as a spherical, isothermal β model. From this analysis we determine the distances to 18 galaxy clusters. Together, these

distances imply a Hubble constant of

$$H_0 = \begin{cases} 60^{+4}_{-4} \text{ km s}^{-1} \text{ Mpc}^{-1}, & \Omega_M = 0.3, \Omega_\Lambda = 0.7, \\ 56^{+4}_{-4} \text{ km s}^{-1} \text{ Mpc}^{-1}, & \Omega_M = 0.3, \Omega_\Lambda = 0.0, \\ 54^{+4}_{-3} \text{ km s}^{-1} \text{ Mpc}^{-1}, & \Omega_M = 1.0, \Omega_\Lambda = 0.0, \end{cases} \quad (11)$$

where the uncertainties are statistical followed by systematic at 68.3% confidence. The systematic uncertainties have been added in quadrature and include an 8% (4% in ΔT_0) uncertainty from the absolute calibration of the SZE data, a 10% effective area uncertainty for the PSPC and HRI, a 5% uncertainty from the column density, a 5% ($\simeq 20/\sqrt{18}$) uncertainty due to asphericity, a 10% effect for our assumptions of isothermality, a one-sided -20% effect from possible small-scale clumping in the ICM, a 12% uncertainty from undetected radio sources, a 2% ($\simeq 8/\sqrt{18}$) uncertainty from the kinetic SZE, a 1% uncertainty from primary CMB anisotropies, a -3% effect from radio halos, and a 3% effect from an imprecisely measured primary beam. These systematic uncertainties are summarized in Table 9. We adopt conservative assumptions when gauging the effects of possible systematics. The contributions from asphericity, kinetic SZE, and primary CMB are expected to average out for a large sample.

The measured distances plotted in Figure 7 with the theoretical relation show that A370 is the largest outlier from the theoretical angular diameter distance relation and MS 1137 has the largest distance uncertainty. A370 exhibits an almost 2:1 axial ratio in the knotty north-south elongation of its X-ray image (see Fig. 2). An optical study of this cluster and its member galaxies shows that the cluster is dominated by two giant elliptical galaxies with a projected separation of about $40''$, roughly in the north-south direction (Mellier et al. 1988). In addition, gravitational lens models suggest that A370 has a bimodal mass distribution with the two components separated in a roughly north-south direction (Kneib et al. 1993; Soucail et al. 1988; Smail et al. 1996). The spherical model used is clearly insufficient for the complex structure of this cluster. The uncertainties on the distance to MS 1137 are particularly large since MS 1137 resides in the distant universe ($z = 0.78$), making it difficult to collect large numbers of X-ray photons. Therefore, the uncertainties on the X-ray-driven quantities are large; in particular, the uncertainty on the measured X-ray temperature is the main contributor to the large uncertainty on the angular diameter distance to MS 1137. The large uncertainties on the distances to both A370 and MS 1137 mean that those clusters contribute little weight in the determination of the Hubble constant.

As discussed in § 2, target clusters were originally chosen from a limited sample of known X-ray clusters. We construct subsamples of our cluster sample to explore the robustness of our result and to look for possible biases in our H_0 determination. A description of the subsamples, the number of clusters in each subsample N , the Hubble constant from each subsample, and the χ^2 and reduced χ^2 for the Hubble parameter are summarized in Table 12 for each subsample considered. Only the $\Omega_M = 0.3$, $\Omega_\Lambda = 0.7$ cosmology is considered in this study. Other cosmologies will have similar changes to the best-fit Hubble parameter. Table 12 shows that excluding the largest outlier, A370, has a negligible effect on the determined Hubble parameter. We

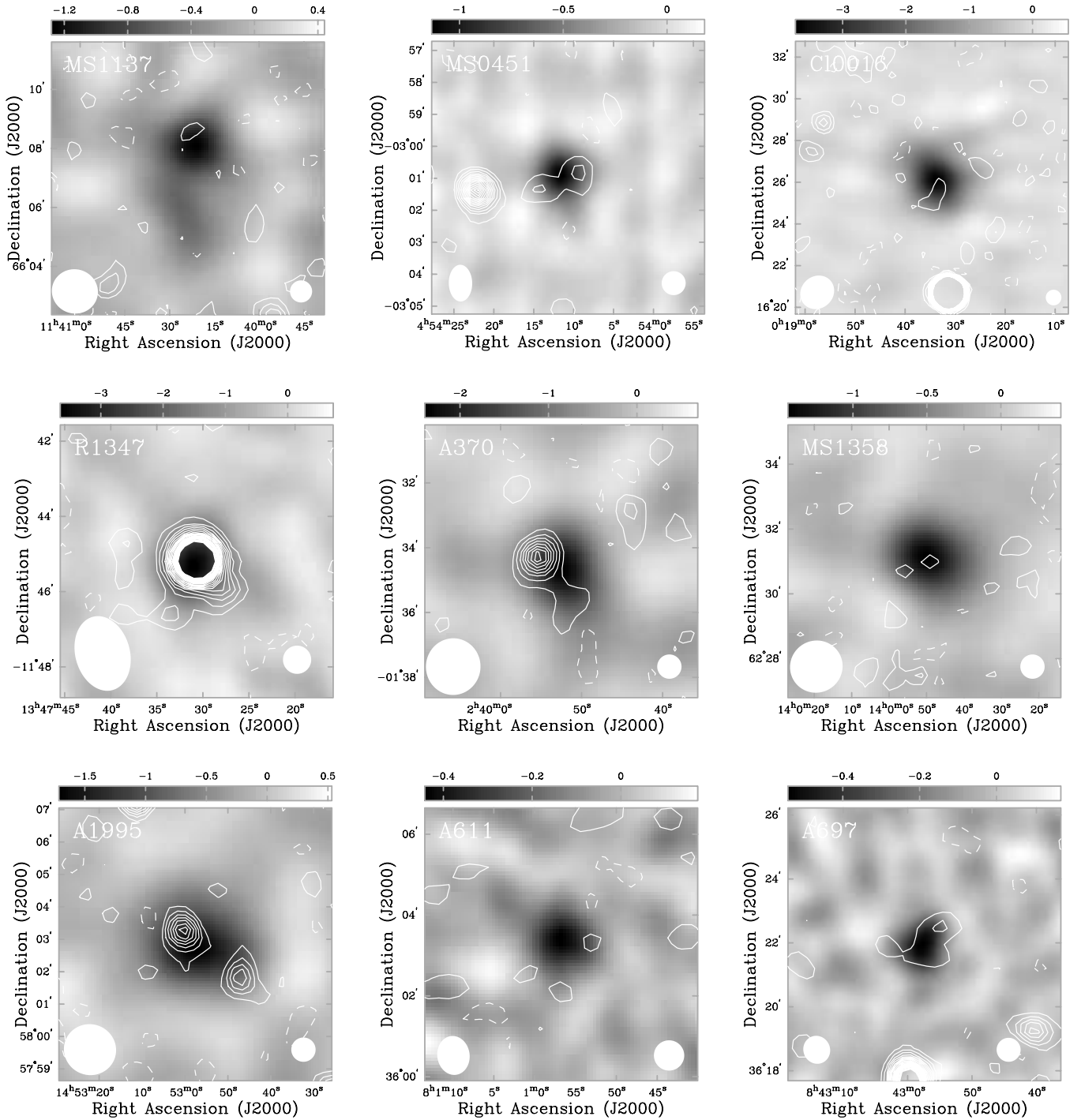
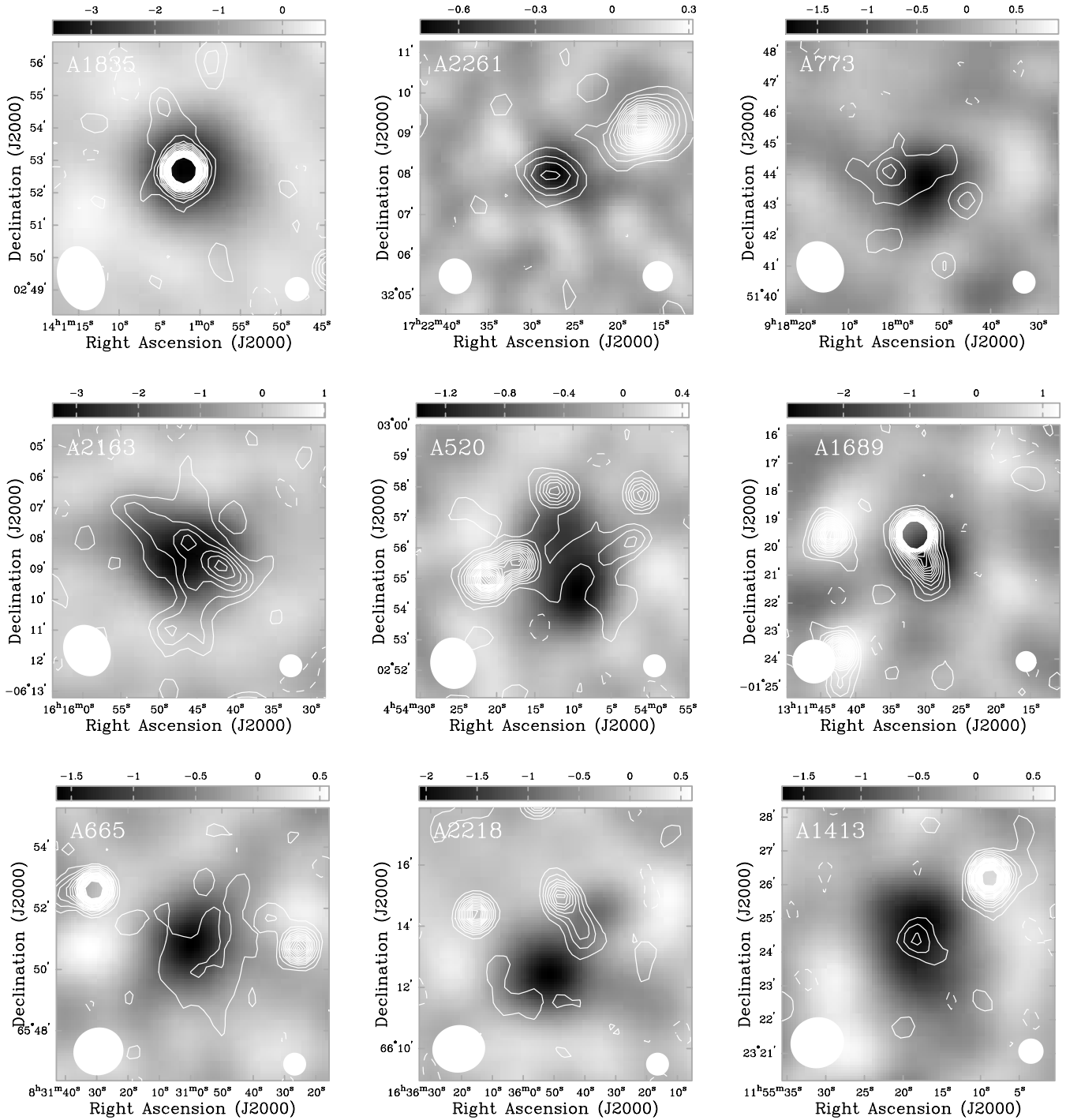


FIG. 9.—SZE from our own 30 GHz observations (*gray scale*) with NVSS 1.4 GHz contours. The 30 GHz images are the gray-scale version of the SZE shown in Fig. 2. The gray-scale wedge above each image shows the range in the flux density of the 30 GHz map in units of mJy beam^{-1} . Contours are multiples of twice the rms, and the NVSS rms is $\sim 0.45 \text{ mJy beam}^{-1}$. The FWHM of the 30 GHz synthesized beam is shown in the lower left-hand corner of each panel, and the $45''$ FWHM beam of the NVSS is shown in the lower right-hand corner of each panel. A2163 exhibits the brightest 1.4 GHz radio halo in our 18 cluster sample. [See the electronic edition of the *Journal* for a color version of this figure.]

also split the sample up based on having a cooling flow, by redshift, presence of a radio halo, based on point sources, based on right ascension and declination, based on X-ray luminosity, and based on membership in the EMSS or being an Abell Cluster.

Jones et al. (2002) constructed an orientation unbiased sample of galaxy clusters for an SZE and X-ray determination of the Hubble parameter. Most importantly, they drew

clusters present in both the BCS (Ebeling et al. 1997, 1998, 2000a; Crawford et al. 1999) and NORAS (Böhringer et al. 2000) surveys with $L_X > 8 \times 10^{44} \text{ ergs s}^{-1}$ and well above the survey flux limits ($> 5 \times 10^{-12} \text{ ergs s}^{-1} \text{ cm}^{-2}$). Eleven clusters satisfy these criteria as well as their redshift range choice ($0.14 \leq z \leq 0.30$) and declination constraint ($\geq 2^\circ$). They find five of the 11 to be sufficiently free from point sources at 15 GHz for SZE measurements. Six of these 11

FIG. 9.—*Continued*

are part of our sample, which we call our orientation unbiased subsample in Table 12.

All of these subsamples yield a Hubble constant with 1σ statistical uncertainties consistent with the H_0 from the entire 18 cluster sample. This argues in favor of a robust H_0 determination.

We compare our results with other SZE-determined distances to clusters in our sample in Table 13. Only statistical uncertainties are included. There are nine clusters in our sample that also have previously determined SZE distances. All of the 1σ confidence regions agree with our own, with

the exception of Cl 0016, R1347, A773, and A665. The systematic uncertainties on the angular diameter distance are $\gtrsim 30\%$ for one galaxy cluster. Therefore, all of the distances are in reasonably good agreement, even after accounting for shared systematics (namely, most use *ROSAT* X-ray data and *ASCA* X-ray temperatures).

Many of the systematics can be approached and reduced through improved observations. For example, *Chandra* and *XMM-Newton* are now producing temperature profiles of galaxy clusters (e.g., Markevitch et al. 2000; Nevalainen et al. 2000; Tamura et al. 2001). The unprecedented angular

TABLE 12
 H_0 FROM DIFFERENT SUBSAMPLES FOR THE Λ COSMOLOGY

Subsample	N	H_0 (km s ⁻¹ Mpc ⁻¹)	χ^2	$\chi^2_{\text{red}}^a$
All.....	18	60 ⁺⁴ ₋₄	16.5	0.97
No A370	17	61 ⁺⁴ ₋₄	10.8	0.68
No MS 1137 or A370.....	16	61 ⁺⁵ ₋₄	9.8	0.65
No cooling flow.....	11	59 ⁺⁶ ₋₅	14.5	1.45
Only cooling flow	7	63 ⁺⁷ ₋₆	1.7	0.28
$z > 0.27$	9	62 ⁺⁷ ₋₆	9.7	1.21
$z < 0.27$	9	59 ⁺⁶ ₋₅	6.6	0.83
No point sources.....	4	53 ⁺⁹ ₋₇	3.4	1.13
Only point sources	14	62 ⁺⁵ ₋₄	12.2	0.94
Only radio halo	6	56 ⁺⁸ ₋₆	6.7	1.34
No halo.....	12	62 ⁺⁵ ₋₅	9.3	0.85
R.A. < 11.5 ^h	9	61 ⁺⁷ ₋₆	13.6	1.70
R.A. > 11.5 ^h	9	60 ⁺⁶ ₋₅	2.9	0.36
Decl. > 30°	9	60 ⁺⁷ ₋₆	8.3	1.04
Decl. < 30°	9	61 ⁺⁶ ₋₅	8.1	1.01
$L_X > 14.5 \times 10^{44}$ ergs s ⁻¹	9	63 ⁺⁶ ₋₅	4.4	0.55
$L_X \leq 14.5 \times 10^{44}$ ergs s ⁻¹	9	57 ⁺⁷ ₋₅	11.5	1.44
EMSS clusters.....	5	66 ⁺¹⁰ ₋₈	3.5	0.88
Abell clusters	13	58 ⁺⁵ ₋₄	12.2	1.02
Orientation unbiased	6	58 ⁺⁸ ₋₆	6.2	1.24

^a $\chi^2_{\text{red}} = \chi^2/(N - 1)$, where $N - 1$ is the degrees of freedom.

resolution of *Chandra* will provide insight into possible clumping in clusters. The effects of undetected point sources are being addressed with multiwavelength (5 and 8 GHz) VLA observations of many of our cluster fields. In addition, there is a project to produce a $\sim 1\%$ calibration of the modified OVRO and BIMA SZE systems, and the current generation of X-ray satellites will reduce the X-ray absolute calibration uncertainty to the few percent level.

The 18 cluster distances presented here are beginning to probe the shape of the angular diameter distance relation. Moreover, constructing subsamples from our 18 cluster sample based on such considerations as cooling flows, redshift, and X-ray luminosity does not significantly affect the best-fit H_0 , suggesting a robust determination of the Hubble parameter. Systematics currently dominate the uncertainty in our determination of the Hubble parameter. These systematics can and will be addressed with current radio observatories (OVRO, BIMA, and VLA) and X-ray satellites (*Chandra* and *XMM-Newton*). With a sample of high-redshift galaxy clusters, this method can be used to constrain the geometry of the universe, providing a valuable independent check of the recent Type Ia supernova (Schmidt et al. 1998; Riess et al. 1998; Perlmutter et al. 1999; Goobar et al. 2000) and primary CMB power spectrum results (Pryke et al. 2002; de Bernardis et al. 2002; Stompor et al. 2001). We emphasize that SZE- and X-ray-determined distances are independent of the extragalactic distance ladder and do not rely on clusters being standard candles or rulers.

A complete review of other distance determination methods is beyond the scope of this paper. We just touch on a few methods that complement SZE-determined distances. The SZE-derived distances are direct, making them an interesting check of the cosmological distance ladder. Our measurement of H_0 in the distant universe agrees within the uncertainties with the *Hubble Space Telescope* (HST) H_0 Key Project results, which probe the

TABLE 13
 COMPARISON OF SZE-DETERMINED DISTANCES

Cluster	D_A^a (Mpc)	References
Cl 0016.....	2041 \pm 499	1
	1788 \pm 664	2
	1100 \pm 295	3
R1347	1221 \pm 356	1
	1890 \pm 644	4
	1897 \pm 401	5
A697	998 \pm 274	1
	1044 \pm 239	6
A1835	1027 \pm 196	1
	867 \pm 411	7
A773	1450 \pm 347	1
	1002 \pm 257	8
A2163	828 \pm 193	1
	728 \pm 387	9
	615 \pm 327	10
A665	466 \pm 198	1
	1017 \pm 229	11
A2218	1029 \pm 346	1
	616 \pm 118	12
	720 \pm 422	13
	1201 \pm 343	6
A1413	573 \pm 161	1
	565 \pm 164	14

^a Includes approximate 68.3% confidence statistical uncertainties only.

REFERENCES.—(1) This paper. (2) Hughes & Birkinshaw 1998. (3) Grainge et al. 2002a. (4) Pointecouteau et al. 2001. (5) Komatsu et al. 1999. (6) Jones et al. 2002. (7) Mäuskopf et al. 2000. (8) Saunders et al. 1999. (9) Holzapfel et al. 1997b. (10) Lamarre et al. 1998. (11) Birkinshaw et al. 1991. (12) Birkinshaw & Hughes 1994. (13) Tsuboi et al. 1998. (14) Grainge et al. 2002b.

nearby universe. The *HST* H_0 Key Project finds $H_0 = 72 \pm 3 \pm 7$ km s⁻¹ Mpc⁻¹ (Freedman et al. 2001), where the uncertainties are statistical followed by systematic at 68.3% confidence. Although few in number, there are other methods that yield distances that are independent of the extragalactic distance ladder. Recent observations of masers orbiting the nucleus of the nearby galaxy NGC 4258 (Herrnstein et al. 1999) illustrate a method of determining direct distances in the nearby universe. Time delays produced by lensing of QSOs by galaxies are another direct distance indicator that can probe the high-redshift universe (for recent examples see Fassnacht et al. 1999; Biggs et al. 1999; Lovell et al. 1998; Barkana 1997; Schechter et al. 1997).

SZE surveys provide a promising method of detecting high-redshift galaxy clusters (e.g., Holder et al. 2000; Barbosa et al. 1996). These surveys will provide large catalogs of high-redshift galaxy clusters required to determine the geometry of the universe from SZE- and X-ray-determined direct distances.

This work is the thesis work of E. D. R. and benefited from useful discussions from very many people. In particular, we thank Gilbert Holder, Jack Hughes, Carlo Graziani, Sandeep Patel, and Thomas Crawford for useful and stimulating discussions. This project would not have been possible without all of the help and support of both the OVRO

and BIMA staff over many years. In particular, E. D. R. would like to thank D. Woody, S. Scott, R. Lawrence, J. R. Forster (Rick), R. Plambeck (Dick), J. Wirth (Red), M. Warnock, and M. Masters for both helping to keep our observations going and teaching E. D. R. all about the details of each observatory. Dave, Rick, and Dick have been especially patient teachers. We would also like to thank the staff of the High Energy Astrophysics Science Archive Research Center (HEASARC). They have always responded promptly, politely, and informatively to our many inquiries over the past few years. In particular, Michael Corcoran and Michael Arida have received the brunt of our questions and have been most helpful. This

work is supported by NASA LTSA grant NAG 5-7986. E. D. R. acknowledges support from NASA GSRP Fellowship NGT 5-50173 and the NASA Chandra Postdoctoral Fellowship PF 1-20020. This research has made use of data obtained through the High Energy Astrophysics Science Archive Research Center on-line service, provided by the NASA Goddard Space Flight Center. This work has also made use of the on-line NVSS and FIRST catalogs operated by the NRAO as well as the NASA/IPAC Extragalactic Database (NED), which is operated by the Jet Propulsion Laboratory, California Institute of Technology, under contract with the National Aeronautics and Space Administration.

REFERENCES

- Allen, S. W. 2000, *MNRAS*, 315, 269
 Allen, S. W., & Fabian, A. C. 1998a, *MNRAS*, 297, L57
 ———. 1998b, *MNRAS*, 297, L63
 Arnaud, M., & Evvard, A. E. 1999, *MNRAS*, 305, 631
 Barbosa, D., Bartlett, J. G., Blanchard, A., & Oukbir, J. 1996, *A&A*, 314, 13
 Barkana, R. 1997, *ApJ*, 489, 21
 Biggs, A. D., Browne, I. W. A., Helbig, P., Koopmans, L. V. E., Wilkinson, P. N., & Perley, R. A. 1999, *MNRAS*, 304, 349
 Birkinshaw, M. 1999, *Phys. Rep.*, 310, 97
 Birkinshaw, M., & Hughes, J. P. 1994, *ApJ*, 420, 33
 Birkinshaw, M., Hughes, J. P., & Arnaud, K. A. 1991, *ApJ*, 379, 466
 Blasi, P., & Colafrancesco, S. 1999, *ASTROPART. Phys.*, 12, 169
 Böhringer, H., et al. 2000, *ApJS*, 129, 435
 Cannon, D. B., Ponman, T. J., & Hobbs, I. S. 1999, *MNRAS*, 302, 9
 Carlstrom, J. E., Grego, L., Holzappel, W. L., & Joy, M. 1998, *Eighteenth Texas Symposium on Relativistic Astrophysics and Cosmology*, ed. A. Olinto, J. Frieman, & D. Schramm (Singapore: World Scientific), 261
 Carlstrom, J. E., Joy, M., & Grego, L. 1996, *ApJ*, 456, L75
 Carlstrom, J. E., Joy, M., Grego, L., Holder, G., Holzappel, W. L., LaRoque, S., Mohr, J. J., & Reese, E. D. 2000, in *Constructing the Universe with Clusters of Galaxies*, ed. F. Durret & G. Gerbal (Paris: IAP), E43
 Carroll, S. M., Press, W. H., & Turner, E. L. 1992, *ARA&A*, 30, 499
 Cash, W. 1979, *ApJ*, 228, 939
 Cavaliere, A., & Fusco-Femiano, R. 1976, *A&A*, 49, 137
 ———. 1978, *A&A*, 70, 677
 Challinor, A., & Lasenby, A. 1998, *ApJ*, 499, 1
 Colberg, J. M., White, S. D. M., MacFarland, T. J., Jenkins, A., Pearce, F. R., Frenk, C. S., Thomas, P. A., & Couchman, H. M. P. 2000, *MNRAS*, 313, 229
 Condon, J. J., Cotton, W. D., Greisen, E. W., Yin, Q. F., Perley, R. A., Taylor, G. B., & Broderick, J. J. 1998, *AJ*, 115, 1693
 Conroy, M. A., Deponte, J., Moran, J. F., Orszak, J. S., Roberts, W. P., & Schmidt, D. 1993, in *ASP Conf. Ser. 52, Astronomical Data Analysis Software and Systems II*, ed. J. B. R. J. Hanisch & R. J. V. Brissenden (San Francisco: ASP), 238
 Cooray, A. R., Grego, L., Holzappel, W. L., Joy, M., & Carlstrom, J. E. 1998, *AJ*, 115, 1388
 Crawford, C. S., Allen, S. W., Ebeling, H., Edge, A. C., & Fabian, A. C. 1999, *MNRAS*, 306, 857
 Crawford, C. S., Edge, A. C., Fabian, A. C., Allen, S. W., Böhringer, H., Ebeling, H., McMahon, R. G., & Voges, W. 1995, *MNRAS*, 274, 75
 Dawson, K. S., Holzappel, W. L., Carlstrom, J. E., Joy, M., LaRoque, S. J., & Reese, E. D. 2001, *ApJ*, 553, L1
 de Bernardis, P., et al. 2002, *ApJ*, 564, 559
 Dennison, B. 1980, *ApJ*, 239, L93
 Dickey, J. M., & Lockman, F. J. 1990, *ARA&A*, 28, 215
 Dolag, K., & Ensslin, T. A. 2000, *A&A*, 362, 151
 Dolgov, A. D., Hansen, S. H., Pastor, S., & Semikoz, D. V. 2001, *ApJ*, 554, 74
 Donahue, M. 1996, *ApJ*, 468, 79
 Donahue, M., Voit, G. M., Scharf, C. A., Gioia, I. M., Mullis, C. R., Hughes, J. P., & Stocke, J. T. 1999, *ApJ*, 527, 525
 Dressler, A., & Gunn, J. E. 1992, *ApJS*, 78, 1
 Ebeling, H., Edge, A. C., Allen, S. W., Crawford, C. S., Fabian, A. C., & Huchra, J. P. 2000a, *MNRAS*, 318, 333
 Ebeling, H., Edge, A. C., Böhringer, H., Allen, S. W., Crawford, C. S., Fabian, A. C., Voges, W., & Huchra, J. P. 1998, *MNRAS*, 301, 881
 Ebeling, H., Edge, A. C., Fabian, A. C., Allen, S. W., Crawford, C. S., & Böhringer, H. 1997, *ApJ*, 479, L101
 Ebeling, H., Edge, A. C., & Henry, J. P. 2001, *ApJ*, 553, 668
 Ebeling, H., Voges, W., Böhringer, H., Edge, A. C., Huchra, J. P., & Briel, U. G. 1996a, *MNRAS*, 281, 799
 ———. 1996b, *MNRAS*, 283, 1103
 Ebeling, H., et al. 2000b, *ApJ*, 534, 133
 Elbaz, D., Arnaud, M., & Böhringer, H. 1995, *A&A*, 293, 337
 Ensslin, T. A., Biermann, P. L., Klein, U., & Kohle, S. 1998, *A&A*, 332, 395
 Fabian, A. C. 1994, *ARA&A*, 32, 277
 Fabian, A. C., Mushotzky, R. F., Nulsen, P. E. J., & Peterson, J. R. 2001, *MNRAS*, 321, L20
 Fairley, B. W., Jones, L. R., Scharf, C., Ebeling, H., Perlman, E., Horner, D., Wegner, G., & Malkan, M. 2000, *MNRAS*, 315, 669
 Fassnacht, C. D., Pearson, T. J., Readhead, A. C. S., Browne, I. W. A., Koopmans, L. V. E., Myers, S. T., & Wilkinson, P. N. 1999, *ApJ*, 527, 498
 Fixsen, D. J., Cheng, E. S., Gales, J. M., Mather, J. C., Shafer, R. A., & Wright, E. L. 1996, *ApJ*, 473, 576
 Freedman, W. L., et al. 2001, *ApJ*, 553, 47
 Geller, M. J., & Beers, T. C. 1982, *PASP*, 94, 421
 Gioia, I. M., & Luppino, G. A. 1994, *ApJS*, 94, 583
 Gioia, I. M., Maccacaro, T., Schild, R. E., Wolter, A., Stocke, J. T., Morris, S. L., & Henry, J. P. 1990, *ApJS*, 72, 567
 Giovannini, G., & Feretti, L. 2000, *NewA*, 5, 335
 Giovannini, G., Tordi, M., & Feretti, L. 1999, *NewA*, 4, 141
 Girardi, M., Fadda, D., Escalera, E., Giuricin, G., Mardirossian, F., & Mezzetti, M. 1997, *ApJ*, 490, 56
 Gómez, P. L., Hughes, J. P., & Birkinshaw, M. 2000, *ApJ*, 540, 726
 Goobar, A., et al. 2000, *Phys. Scr.*, 85, 47
 Gould, R. J. 1980, *ApJ*, 238, 1026
 Grainge, K., Grainger, W. F., Jones, M. E., Kneissl, R., Pooley, G. G., & Saunders, R. 2002a, *MNRAS*, 329, 890
 Grainge, K., Jones, M., Pooley, G., Saunders, R., & Edge, A. 1993, *MNRAS*, 265, L57
 Grainge, K., Jones, M. E., Pooley, G., Saunders, R., Edge, A., & Kneissl, R. 2002b, *MNRAS*, 333, 318
 Grego, L., Carlstrom, J. E., Joy, M. K., Reese, E. D., Holder, G. P., Patel, S., Cooray, A. R., & Holzappel, W. L. 2000, *ApJ*, 539, 39
 Grego, L., Carlstrom, J. E., Reese, E. D., Holder, G. P., Holzappel, W. L., Joy, M. K., Mohr, J. J., & Patel, S. 2001, *ApJ*, 552, 2
 Hanisch, R. J. 1982, *A&A*, 116, 137
 Herbig, T., Lawrence, C. R., Readhead, A. C. S., & Gulkis, S. 1995, *ApJ*, 449, L5
 Herrnstein, J. R., et al. 1999, *Nature*, 400, 539
 Holder, G. P., Mohr, J. J., Carlstrom, J. E., Evvard, A. E., & Leitch, E. M. 2000, *ApJ*, 544, 629
 Holzappel, W. L., Ade, P. A. R., Church, S. E., Mauskopf, P. D., Rephaeli, Y., Wilbanks, T. M., & Lange, A. E. 1997a, *ApJ*, 481, 35
 Holzappel, W. L., Carlstrom, J. E., Grego, L., Holder, G., Joy, M., & Reese, E. D. 2000, *ApJ*, 539, 57
 Holzappel, W. L., et al. 1997b, *ApJ*, 480, 449
 Hughes, J. P., & Birkinshaw, M. 1998, *ApJ*, 501, 1
 Inagaki, Y., Sugimoto, T., & Suto, Y. 1995, *PASJ*, 47, 411
 Itoh, N., Kohyama, Y., & Nozawa, S. 1998, *ApJ*, 502, 7
 Jaffe, W. J. 1977, *ApJ*, 212, 1
 ———. 1980, *ApJ*, 241, 925
 Jones, L. R., Scharf, C., Ebeling, H., Perlman, E., Wegner, G., Malkan, M., & Horner, D. 1998, *ApJ*, 495, 100
 Jones, M., et al. 1993, *Nature*, 365, 320
 ———. 2002, *MNRAS*, submitted
 Kaloglyan, A. T., Nanni, D., & Vignato, A. 1990, *Astrophysics*, 31, 672
 Kempner, J. C., & Sarazin, C. L. 2001, *ApJ*, 548, 639
 Kendall, M., & Stuart, A. 1979, in *The Advanced Theory of Statistics*, Vol. 2: Inference and Relationship (4th ed.; London: Griffin), 246
 Kneib, J. P., Mellier, Y., Fort, B., & Mathez, G. 1993, *A&A*, 273, 367
 Kneib, J. P., Mellier, Y., Pello, R., Miralda-Escude, J., Le Borgne, J., Böhringer, H., & Picat, J. 1995, *A&A*, 303, 27
 Kolb, E. W., & Turner, M. S. 1990, *Frontiers in Physics* (Reading: Addison-Wesley)
 Komatsu, E., Kitayama, T., Suto, Y., Hattori, M., Kawabe, R., Matsuo, H., Schindler, S., & Yoshikawa, K. 1999, *ApJ*, 516, L1
 Lamarre, J. M., et al. 1998, *ApJ*, 507, L5

- Le Borgne, J. F., Pello, R., & Sanahuja, B. 1992, *A&AS*, 95, 87
- Liang, H., Hunstead, R. W., Birkinshaw, M., & Andreani, P. 2000, *ApJ*, 544, 686
- Lovell, J. E. J., Jauncey, D. L., Reynolds, J. E., Wieringa, M. H., King, E. A., Tzioumis, A. K., McCulloch, P. M., & Edwards, P. G. 1998, *ApJ*, 508, L51
- Maccacaro, T., Wolter, A., McLean, B., Gioia, I. M., Stocke, J. T., della Ceca, R., Burg, R., & Faccini, R. 1994, *Astrophys. Lett.*, 29, 267
- Majumdar, S., & Nath, B. B. 2000, *ApJ*, 542, 597
- Markevitch, M. 1997, *ApJ*, 483, L17
- Markevitch, M., Mushotzky, R., Inoue, H., Yamashita, K., Furuzawa, A., & Tawara, Y. 1996, *ApJ*, 456, 437
- Markevitch, M., et al. 2000, *ApJ*, 541, 542
- Mason, B. S. 1999, Ph.D. thesis, Univ. Pennsylvania
- Mason, B. S., Myers, S. T., & Readhead, A. C. S. 2001, *ApJ*, 555, L11
- Mathiesen, B., Evrard, A. E., & Mohr, J. J. 1999, *ApJ*, 520, L21
- Mauskopf, P. D., et al. 2000, *ApJ*, 538, 505
- Mellier, Y., Soucail, G., Fort, B., & Mathez, G. 1988, *A&A*, 199, 13
- Moffet, A. T., & Birkinshaw, M. 1989, *AJ*, 98, 1148
- Mohr, J. J., Evrard, A. E., Fabricant, D. G., & Geller, M. J. 1995, *ApJ*, 447, 8
- Mohr, J. J., Mathiesen, B., & Evrard, A. E. 1999, *ApJ*, 517, 627
- Molnar, S. M., & Birkinshaw, M. 1999, *ApJ*, 523, 78
- Mushotzky, R. F., & Scharf, C. A. 1997, *ApJ*, 482, L13
- Myers, S. T., Baker, J. E., Readhead, A. C. S., Leitch, E. M., & Herbig, T. 1997, *ApJ*, 485, 1
- Nagai, D., & Mohr, J. J. 2002, *ApJ*, submitted
- Nagai, D., Sulkanen, M. E., & Evrard, A. E. 2000, *MNRAS*, 316, 120
- Nevalainen, J., Markevitch, M., & Forman, W. 2000, *ApJ*, 536, 73
- Ota, N., Mitsuda, K., & Fukazawa, Y. 1998, *ApJ*, 495, 170
- Patel, S. K., et al. 2000, *ApJ*, 541, 37
- Peacock, J. A. 1999, *Cosmological Physics* (Cambridge: Cambridge Univ. Press)
- Pearson, T. J., Shepherd, M. C., Taylor, G. B., & Myers, S. T. 1994, *BAAS*, 185, 0808
- Peres, C. B., Fabian, A. C., Edge, A. C., Allen, S. W., Johnstone, R. M., & White, D. A. 1998, *MNRAS*, 298, 416
- Perlmutter, S., et al. 1999, *ApJ*, 517, 565
- Peterson, J. R., et al. 2001, *A&A*, 365, L104
- Pointecouteau, E., Giard, M., Benoit, A., Désert, F. X., Aghanim, N., Coron, N., Lamarre, J. M., & Delabrouille, J. 1999, *ApJ*, 519, L115
- Pointecouteau, E., Giard, M., Benoit, A., Désert, F. X., Bernard, J. P., Coron, N., & Lamarre, J. M. 2001, *ApJ*, 552, 42
- Pospieszalski, M. W., Lakatos, W. J., Nguyen, L. D., Lui, M., Liu, T., Le, M., Thompson, M. A., & Delaney, M. J. 1995, *IEEE MTT-S Int. Microwave Symp.*, 1121
- Pryke, C., Halverson, N. W., Leitch, E. M., Kovac, J., Carlstrom, J. E., Holzapfel, W. L., & Dragovan, M. 2002, *ApJ*, 568, 46
- Raymond, J. C., & Smith, B. W. 1977, *ApJS*, 35, 419
- Reese, E. D., et al. 2000, *ApJ*, 533, 38
- Rephaeli, Y. 1995, *ApJ*, 445, 33
- Rephaeli, Y., & Yankovitch, D. 1997, *ApJ*, 481, L55
- Riess, A. G., et al. 1998, *AJ*, 116, 1009
- Roettiger, K., Stone, J. M., & Mushotzky, R. F. 1997, *ApJ*, 482, 588
- Roland, J. 1981, *A&A*, 93, 407
- Rudy, D. J. 1987, Ph.D. thesis, Caltech
- Sault, R. J., Teuben, P. J., & Wright, M. C. H. 1995, in *ASP Conf. Ser. 77, Astronomical Data Analysis Software and Systems IV*, ed. R. A. Shaw, H. E. Payne, & J. J. E. Hayes (San Francisco: ASP), 433
- Saunders, R., et al. 1999, *MNRAS*, submitted
- Sazonov, S. Y., & Sunyaev, R. A. 1998a, *ApJ*, 508, 1
- . 1998b, *Astron. Lett.*, 24, 553
- Scharf, C. A., Jones, L. R., Ebeling, H., Perlman, E., Malkan, M., & Wegner, G. 1997, *ApJ*, 477, 79
- Schechter, P. L., et al. 1997, *ApJ*, 475, L85
- Schindler, S., Hattori, M., Neumann, D. M., & Böhringer, H. 1997, *A&A*, 317, 646
- Schindler, S., et al. 1995, *A&A*, 299, L9
- Schlickeiser, R., Sievers, A., & Thiemann, H. 1987, *A&A*, 182, 21
- Schmidt, B. P., et al. 1998, *ApJ*, 507, 46
- Scoville, N. Z., Carlstrom, J. E., Chandler, C. J., Phillips, J. A., Scott, S. L., Tilanus, R. P. J., & Wang, Z. 1993, *PASP*, 105, 1482
- Smail, I., Dressler, A., Kneib, J., Ellis, R. S., Couch, W. J., Sharples, R. M., & Oemler, A. J. 1996, *ApJ*, 469, 508
- Soucail, G., Mellier, Y., Fort, B., Mathez, G., & Cailloux, M. 1988, *A&A*, 191, L19
- Stebbins, A. 1997, preprint (astro-ph/9709065)
- Stocke, J. T., Morris, S. L., Gioia, I. M., Maccacaro, T., Schild, R., Wolter, A., Fleming, T. A., & Henry, J. P. 1991, *ApJS*, 76, 813
- Stomp, R., et al. 2001, *ApJ*, 561, L7
- Struble, M. F., & Rood, H. J. 1991, *ApJS*, 77, 363
- . 1999, *ApJS*, 125, 35
- Sulkanen, M. E. 1999, *ApJ*, 522, 59
- Sunyaev, R. A., & Zeldovich, Ya. B. 1970, *Comments Astrophys. Space Phys.*, 2, 66
- . 1972, *Comments Astrophys. Space Phys.*, 4, 173
- Tamura, T., et al. 2001, *A&A*, 365, L87
- Tsuboi, M., Miyazaki, A., Kasuga, T., Matsuo, H., & Kuno, N. 1998, *PASJ*, 50, 169
- Watkins, R. 1997, *MNRAS*, 292, L59
- Worrall, D. M., et al. 1992, in *Data Analysis in Astronomy IV*, ed. V. Di Gesù et al. (New York: Plenum Press), 145